Surface & Coatings Technology 512 (2025) 132376

Contents lists available at ScienceDirect

Surface & Coatings Technology

journal homepage: www.elsevier.com/locate/surfcoat

Investigation of the temperature-dependent failure processes in PVD Cr-coated ZIRLO nuclear fuel cladding using *in situ* X-ray micro-tomography imaging

Guanjie Yuan [a,b], Martin Ševeček [c,d], David Cook [e], Dula Parkinson [f], Robert O. Ritchie [e,g], Dong Liu [a,b,*]

[a] Department of Engineering Science, University of Oxford, Oxford, UK
[b] School of Physics, University of Bristol, Bristol, UK
[c] Department of Nuclear Science and Engineering, Massachusetts Institute of Technology, Cambridge, MA, USA
[d] Faculty of Nuclear Sciences and Physical Engineering, Czech Technical University in Prague, Prague, Czech Republic
[e] Department of Materials Science & Engineering, University of California Berkeley, BA, USA
[f] Advanced Light Source, Lawrence Berkeley National Laboratory, Berkeley, CA, USA
[g] Materials Sciences Division, Lawrence Berkeley National Laboratory, Berkeley, CA, USA

ARTICLE INFO

Keywords:
Accident tolerant fuel
Chromium coating
Physical vapour deposition
C-ring compression
X-ray computed micro-tomography

ABSTRACT

In this work, an accident tolerant fuel cladding system with Cr coating deposited using physical vapour deposition (PVD) method onto commercial Optimized ZIRLO™ was studied. The cladding tubes were machined into C-rings and loaded to failure under compression with real-time synchrotron micro-X-ray computed tomography (XCT) imaging at room temperature (RT), 345 °C, 650 °C and 950 °C in argon (Ar) atmosphere. The mechanical behaviour and failure processes were found strongly temperature-dependent where the Cr coating showed brittle fracture at RT and 345 °C, ductile fracture at 650 °C and a reversion to brittle fracture at 950 °C. Nano-indentation measurements and scanning electron microscopy (SEM) imaging were conducted on the materials after high temperature testing. It was found that recrystallisation of the Cr coating occurred at elevated temperatures, which significantly affected its local properties hence the failure behaviour at different temperatures. This work represents the first *in situ* 3D XCT observation of progressive failure processes in PVD Cr-coated ZIRLO claddings up to 950 °C providing critical insights into its brittle-to-ductile transition (BDTT) behaviour and subsequent ductile-to-brittle reversion with the increase in temperature. Moreover, results are compared with other PVD Cr-coated Zircaloy materials from open literature; the influences of the coating microstructure and local properties on the failure stress/strain and fracture processes are discussed.

1. Introduction

Zr-based alloys (Zircaloys) have been widely used as fuel cladding materials in light water reactors (LWRs) for decades, due to their high melting point (1852 °C), low neutron absorption, excellent corrosion resistance and mechanical properties [1]. To enhance the corrosion resistance, reduce the hydrogen pickup and improve the dimensional stability of the Zircaloys, ZIRLO® was developed by Sabol et al. in 1987 [2]. Optimized ZIRLO® (Opt. ZIRLO™) was subsequently developed by Westinghouse Electric Company LLC with further improved corrosion resistance and creep resistance [3].

However, Zircaloys can rapidly oxidise when exposed to high-temperature steam. This causes serious degradation of its strength and loss of structural integrity of Zircaloys which also release combustible hydrogen gas as well as heat [4], *e.g.*, in the 2011 Fukushima-Daiichi disaster [5]. Subsequently, concept of accident tolerant fuels (ATFs) has been formally proposed [5]. The primary objective of ATFs is to tolerate a severe accident in the reactor core for a longer period than the current UO_2-Zircaloy fuel system, while maintaining or improving the fuel performance during normal operations and operational transients [6]. Regarding Zircaloy claddings, the primary objective is to delay or reduce the oxidation rate of Zircaloy under severe accident conditions. For instance, when Zircaloy is exposed to steam at 1200 °C (representative of loss of coolant accident (LOCA) conditions) [7], the oxide layer

* Corresponding author.
E-mail address: dong.liu@eng.ox.ac.uk (D. Liu).

https://doi.org/10.1016/j.surfcoat.2025.132376
Received 17 April 2025; Received in revised form 3 June 2025; Accepted 4 June 2025
Available online 6 June 2025

growth rate is ~10 to 50 μm/min, accompanied by a weight gain of ~200 to 300 mg/cm^2 within the initial 1–2 h of exposure. The objective is to achieve a reduction in the oxide layer growth rate to approximately 1 to 5 μm/min and limit the weight gain to approximately 50 to 100 mg/cm^2 under comparable conditions [8,9]. Consequently, the application of a protective coating layer on the outer cladding surface has been proposed [4]. Cr has remarkable advantages (*e.g.*, high oxidation resistance, good chemical compatibility with Zircaloy materials [4]), and has been chosen as the protective coating material on current Zircaloy claddings in LWRs.

Various methods have been used to deposit Cr coating on the Zircaloy cladding, *e.g.*, cold spraying (CS), 3D laser melt-coating and physical vapour deposition (PVD) [10]. Among them, PVD process has notable advantages and it is a widely studied coating on Zircaloy materials [11–13]. During the PVD process, Cr particles are vapourised into gaseous particles, and subsequently deposited onto the substrate [14]. PVD process can be achieved at relatively low deposition temperatures (below 500 °C, and can even be achieved at room temperature (RT)), and it has the ability to precisely control coating quality by adjusting flexible and controllable manufacturing parameters [15]. Typical PVD Cr coating has fine Cr grains clustered close to the coating/substrate interface region with larger columnar Cr grains grows towards outside surface of the coating. It has been widely reported that the PVD process does not introduce any obvious plastic deformation to the underlying substrate (commonly occurs during CS process at the coating/substrate interface region) or cause changes in the mechanical properties of the substrate, resulting in relatively smooth coating/substrate interfaces [4]. For example, Hong et al. [16] reported in a PVD Cr-coated Opt. ZIRLO™ cladding material, the elastic modulus and hardness of substrate close to the interface area (6 μm or less distance away from the interface) are similar to that away from the interface: ~95.5 GPa and ~3.1 GPa.

Various studies have been conducted to investigate the mechanical behaviour of the PVD Cr-coated Zircaloy materials at elevated temperatures. *In situ* 2D scanning electron microscope (SEM) imaging combined with mechanical loading has been used recently to investigate the failure processes of such material in real-time. For instance, Jiang et al. [12] conducted *in situ* tensile tests of PVD Cr-coated Zircaloy-4 sheet specimens (~15 μm of coating thickness) up to 500 °C. The tensile strength was reported to decrease with temperature (~430 MPa at RT to ~170 MPa at 500 °C), and the tensile strains at the initiation of coating cracks was found to increase with temperature (~0.44 % at RT to ~13 % at 500 °C). However, such 2D SEM imaging could only provide information of either cracks on the surface of the sample, or cross-sections at the edge of the sample; without providing any 3D information of the pathways of cracks in the coating/substrate system. These mechanical tests combined with real-time SEM imaging were conducted on sheet specimens exacted along the axial direction of the cladding tube, and the failure stress/strain measured is orthogonal to the maximum hoop tensile stress introduced during service due to internal pressurisation and potential claddings and fuel pellets [17].

Moreover, during servicing in LWRs, the temperature of Zircaloy claddings could rapidly raise to over 950 °C under LOCA and reactivity-initiated accident (RIA) conditions [18], and even above 1200 °C under severe accidents. At such high temperatures, the local properties and microstructures of both Cr coatings and underlying substrate could change, and consequently affect the mechanical behaviour and failure processes of the entire Cr-coated cladding system. Therefore, to facilitate the future industrial application of Cr-coated cladding materials, it is essential to investigate their mechanical behaviour at extreme temperatures. However, authors note that to date, no openly published studies have investigated the real-time failure processes of such PVD Cr-coated Zircaloys claddings under loading at high temperatures over 500 °C. Our previous study has combined C-ring compression loading and real-time X-ray computed micro-tomography (XCT) to investigate the mechanical behaviour and failure processes of a PVD Cr-coated Zircaloy-4 cladding material [4] under hoop tensile stress only up to 345 °C.

In current work, the mechanical behaviour and failure processes of one PVD Cr-coated Opt. ZIRLO™ cladding materials were investigated at elevated temperatures up to 950 °C under C-ring loading with real-time XCT imaging. The microstructures and local properties of the as-received materials and materials after high temperature testing were also studied.

2. Materials and experimental procedures

2.1. Materials

In current study, the Cr-coated Opt. ZIRLO™ cladding material (Fig. 1a) was manufactured *via* PVD method, more specifically unbalanced magnetron sputtering and descriptions of the manufacturing processes can be found in refs [16,19]. One representative schematic of the cross-section of the cladding material is presented in Fig. 1b. The wall-thickness (t), outer radius (r_o) and inner radius (r_i) of the cladding were estimated from XCT imaging, resulting in values of $t = 0.57 \pm 0.017$ mm, $r_o = 4.57 \pm 0.021$ mm and $r_i = 4.00 \pm 0.016$ mm.

2.2. Experiments and sample preparation

Various measurement techniques were utilised including scanning electron microscopy (microstructures imaging), nanoindentation (elastic modulus and hardness measurements), C-ring compression with real-time synchrotron 3D XCT imaging. The detailed experimental setup and corresponding materials preparation are described in Sections 2.2.1 to 2.2.4. The image analysis process for the XCT scans are described in Section 2.2.5.

2.2.1. Samples preparation

For SEM imaging and nanoindentation on the cross-sections of both as-received materials and materials after C-ring compression testing, samples were mounted by a BUEHLER SimpliMet™ XPS1 hot compression mounting machine. It was operated at a pressure of 3 MPa and a temperature of 180 °C, with 180 s for both heating and cooling times. A BUEHLER EcoMet™ 30 Semi-Automatic Grinder Polisher was then used to ground the samples, with 400-grit (~2 mins), 600-grit (~2 mins), 800-grit (~4 mins), 1200-grit (~5 mins), 2500-grit (~5 mins) and 4000-grit (~5 mins) sand grinding discs. The samples were subsequently polished using 3 μm (MD-Nap cloth) and 1 μm (MD-Nap cloth) water-based diamond suspensions, with each polishing step being ~4 mins at a rotation speed of 260 rpm. Finally, the surface of the samples was cleaned in water and ethanol and air-dried for more than 48 h before the tests.

For C-ring compression experiments, a CUTLAM®1.1 manual cutting machine combined with a slow speed diamond saw was used. Claddings were firstly cut by the saw (operated at 230 rpm) into a C-ring geometry.

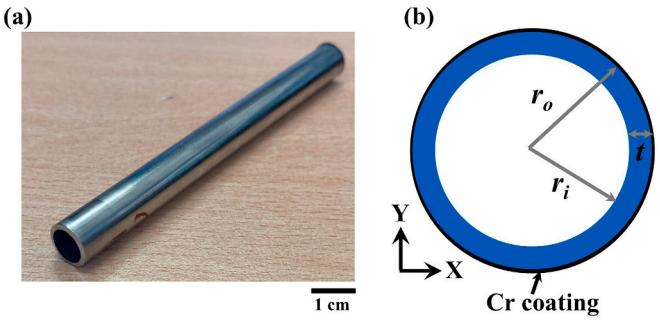

Fig. 1. (a) One picture shows the Cr-coated Opt. ZIRLO™ cladding material. (b) Schematic of the cross-section of the cladding material shows its geometry, where r_i is the inner radius, r_o is the outer radius and t is the wall-thickness of the cladding.

The width of all samples is in the range of ~2.3 mm to ~2.5 mm. All the samples were cleaned by water and ethanol, and air-dried more than 48 h before the experiments. For SEM imaging of the crack patterns after C-ring compression testing, samples were first cleaned by ethanol, and then mounted on to an aluminium SEM specimen pin stubs (AGG301, Agar Scientific) by fast-drying silver suspension (Agar Scientific).

2.2.2. SEM imaging parameters

Zeiss Evo MA10 LaB6 scanning electron microscope was used in current work. For all the samples, the microscope was operated at a current of 62 μA, a 20 kV accelerating voltage, with a working distance of 8.5 to 11.5 mm. The thickness of the Cr coating was also measured by SEM imaging.

2.2.3. Nanoindentation

For nanoindentation measurements, a Hysitron TI Premier nano-indenter with a Berkovich diamond tip (three-sided pyramidal shape) was used. Prior to all the measurements, a tip calibration process was performed using standard fused silica. This process generated a tip area function to correct for any geometrical deviations from the ideal Berkovich shape [5]. The polished specimen cross-sections were mounted on loading stage using a thin layer of crystalbond adhesive. Location of each indent was identified using a 40× objective lens. A depth control was used during the experiment, with both loading and unloading rates of 100 nm s^{-1}, and holding 2 s at a depth of 500 nm. For the areas where multiple indents were conducted, the indents were spaced more than 5 μm apart. Hardness (H) and elastic modulus (E) were calculated using the Oliver and Pharr method [20], from Eqs. (1) and (2), respectively:

$$H = \frac{P_{Max}}{A}, \tag{1}$$

$$\frac{1}{E_r} = \frac{1-\nu_i^2}{E_i} + \frac{1-\nu_s^2}{E}, \tag{2}$$

where P_{Max} is the maximum load (mN), A is the projected contact area, E_r is the reduced modulus of tested materials. E_i and ν_i are respectively elastic modulus (1140 GPa) and Poisson's ratio of the indenter tip (0.07). A ν_s of 0.21 [21] and 0.34 [22] was used for Cr coating and Opt. ZIRLO™ substrate, respectively, in the current work.

2.2.4. Real-time high temperature C-ring compression experiments

In situ high temperature C-ring compression tests combined with XCT imaging were conducted on the cladding materials at Beamline 8.3.2 of the Advanced Light Source at Lawrence Berkeley National Laboratory. As presented in Fig. 2, compressive load was applied to the specimen by using two alumina ceramic plates. The maximum hoop stress (σ_{ymax}) can be calculated from Eq. (3) following the ASTM Standard C1323–16 [23]:

$$\sigma_{ymax} = \frac{P_U R}{b t r_o}\left[\frac{r_o - r_a}{r_a - R}\right] \tag{3}$$

where P_U = peak load, b = width of C-ring sample, average radius r_a and term R are defined by Eqs. (4) and (5), respectively:

$$r_a = \left(\frac{r_o + r_i}{2}\right) \tag{4}$$

$$R = \frac{r_0 - r_i}{ln\frac{r_o}{r_i}} \tag{5}$$

Note that, to prevent the variations of circumferential stress across the entire width (b) of sample, ASTM C1323–16 [23] suggests the b should be no more than twice of the wall-thickness (t). This constraint has been relaxed by Embree et al. [24] based on their finite element analysis (FEA) of various b/t ratio combinations, with detailed results tabulated in Table S1 in the Supplementary Materials. In this work, b/t ratios of all C-ring samples are in the range of 4.0 to 4.4. This indicates, at the outermost surface of the sample, the hoop stress was at least an order of magnitude higher than the axial stress [24] (Fig. 2).

The unique testing facility adopted in current work consists of a mechanical loading system, a heating chamber and a X-ray system [4,5,25–27]. During the test, the loading rig was operated in displacement-control mode. A small pre-load of ~5 N was applied to all tested samples to prevent specimen movement. To apply quasi-static loading to the samples, a loading speed of ~0.5 μm/s was used. Inside heating chamber, there are six 150 W infrared halogen lamps, each equipped with a gold ellipsoidal reflector. The lamps generate a uniform hot zone of ~0.5 cm^3 at the centre of chamber. During each experiment, sample was positioned in this hot zone, with the testing temperature monitored by a thermocouple attached to the outer surface of the sample and controlled by a programmable power supply. For testing at high temperature, experiments were conducted once the temperature stabilized at 345 ± 2 °C, 650 ± 5 °C and 950 ± 5 °C, in argon atmosphere. Two samples were tested at each temperature. And the samples were cooled down in the chamber.

During the test, a white light X-ray beam within energy of 6 to 43 keV was employed. Sets of X-ray projection images were acquired when the test instrument was incrementally rotated through an angular range of 180°. These radiographs were subsequently converted to visible light using a Lutetium Aluminium Garnet scintillator, imaged with a Mitutoyo objective lens (2× long working distance), and recorded on a high-resolution detector (PCO Edge CCD camera, 2560 × 2560 pixels). This setup resulted in a pixel size of 3.25 μm × 3.25 μm and a field of view of 8 mm × 4 mm, on the middle section of the C-ring samples where maximum hoop stress was generated (as indicated by the dashed line in Fig. 1). Each scan involves the collection of 1969 projections, with an acquisition time of 30 ms per projection and a total acquisition time of ~6 mins. For each sample, the total testing time is about 1 h. Real-time radiography projections were used to monitor the position of sample, as well as observe the formation of cracks. For each sample, four to seven XCT scans were collected at increasing loading steps. XCT scans at each loading step were normalised to the peak load and are summarized in Table S3.

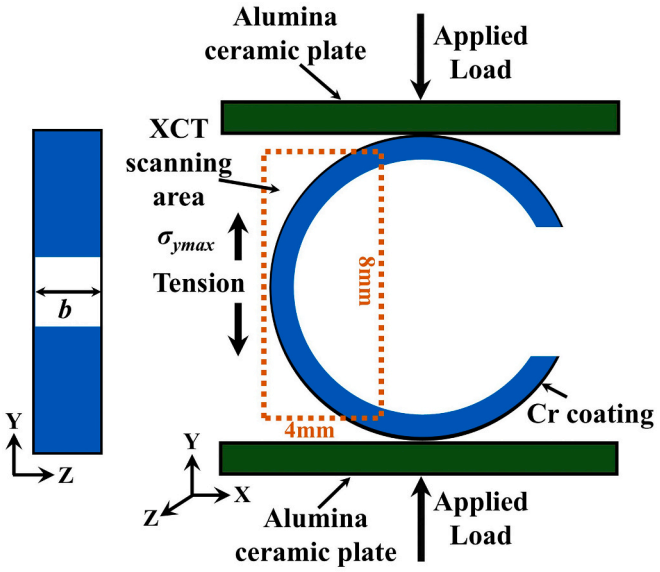

Fig. 2. Schematic of the C-ring compression configuration for real-time XCT testing of cladding materials, including the dimensions of C-ring sample and the coordinate system. b is the width of C-ring sample. The XCT field of view, indicated by the dashed rectangle, is positioned in the region of the sample experiencing maximum tensile stress and strain. X is the radial direction, Y is the hoop direction and Z is along the longitudinal direction of the cladding.

2.2.5. Analysis of the real-time XCT scans for 3D visualisation

The reconstruction of XCT images was carried out using the Gridrec algorithm [28] in the TomoPy package [29]. For each scan, the rotation centre was manually identified to mitigate potential artefacts. To improve spatial resolution and reduce fixed-pattern noise, a conventional flat field correction was applied. The reconstructed scans were converted into stacks of 32-bit tiff images and imported into the open-source software ImageJ [30] to convert them into 8-bit raw data files. These raw data files were then imported into Avizo Lite software (version 2019.4) for 3D visualisation of coating cracks [31]. To minimise the impact of tensile stress variations along the hoop direction of C-ring sample on coating crack behaviours, all reconstructed XCT images were cropped into a specific range. This range encompassed a radial angle of ±30° relative to the sample's middle plane. As reported by Embree et al. [24], in the selected range, similar hoop stress can be found on the outermost surface of the C-ring sample. Therefore, only coating cracks in the selected range were analysed to investigate their formation and progressive propagation.

3. Results

In this section, the results are presented for (i) the microstructures and local properties of as-received materials and the materials after C-ring compression tests (at RT, 345 °C, 650 °C and 950 °C), (ii) mechanical behaviour of the material tested at RT, 345 °C, 650 °C and 950 °C, and (iii) failure processes and crack patterns of the material tested at these temperatures.

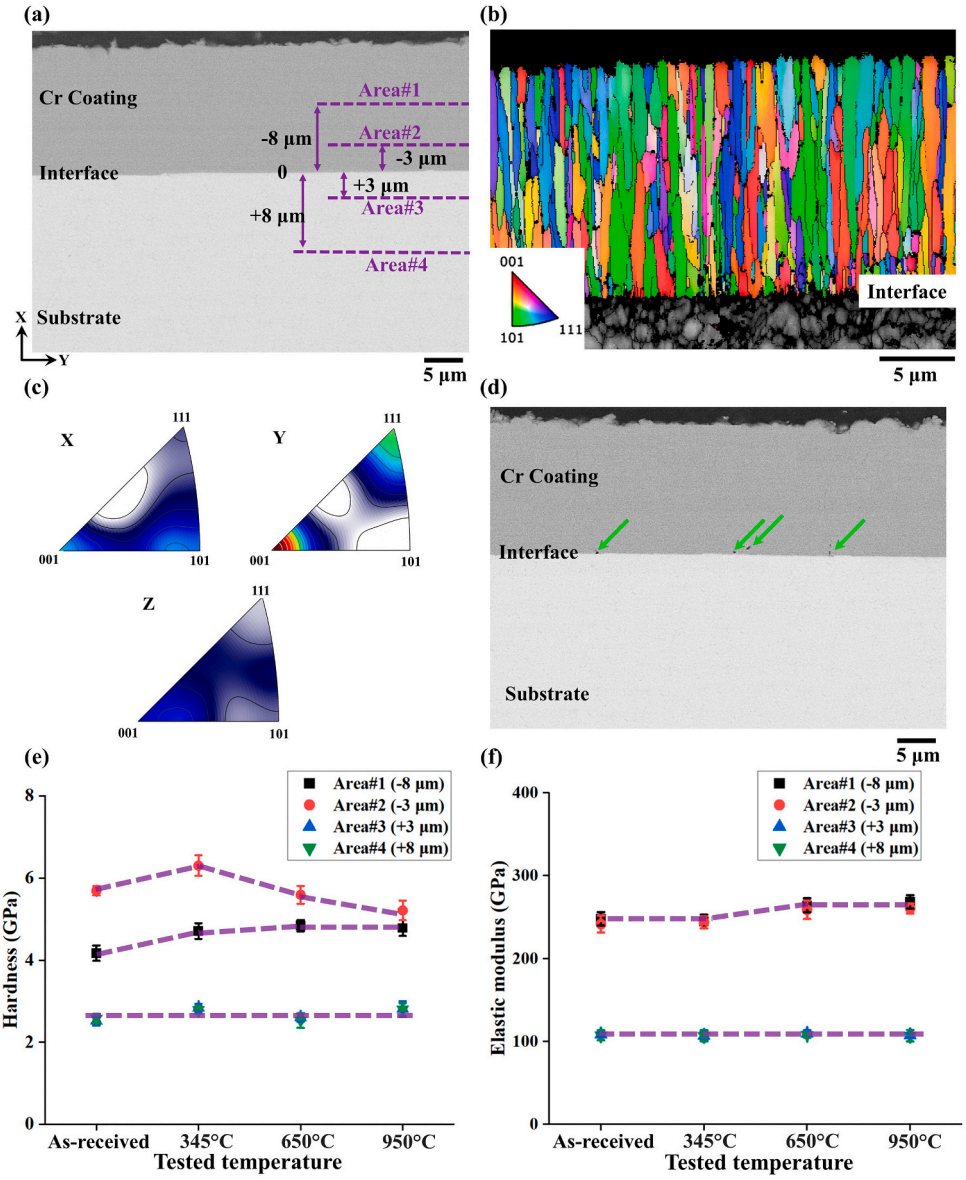

Fig. 3. (a) SEM images collected in BSE mode showing the polished cross-sections of the as-received materials, the linescans where indentation measurements were conducted are marked by dash lines and indicated as 'Area#1' at −8 µm away from the interface, 'Area#2' at −3 µm away from the interface, 'Area#3' at +3 µm away from the interface, and 'Area#1' at +8 µm away from the interface. (b) EBSD mapping of the as-received Cr coating. (c) Inverse pole figures (IPFs) show textures of the Cr grains in the as-received Cr coating based on the EBSD scan in (b). (d) SEM images collected in BSE mode showing the polished cross-sections of materials after testing at 950 °C, with pores marked by green arrows. (e) and (f) are comparisons of hardness (*H*) and elastic modulus (*E*) values of as-received material, and materials after C-ring compression testing at 345 °C, 650 °C and 950 °C. Dashed lines are for eye guidance only. Each data point is an average of more than 20 measurements; the error bars represent standard deviation.

3.1. Microstructures and local properties

The typical microstructure of the as-received material is presented in Fig. 3a. Under current resolution, no obvious pores can be found in the coating and at the coating/substrate interface. The Cr coating/substrate interface was found to be relatively flat. The thickness of the Cr coating was measured to be 15.78 ± 0.42 μm. As presented in Fig. 3b, the Cr grains exhibit a predominantly columnar morphology, with smaller grains localised near the coating/substrate interface. Cr grains were found showing strong texture: the majority of them oriented along the [001] and [111] in the Y direction, Fig. 3c. The average area of the Cr grains was measured to be 1.1 ± 0.8 μm^2.

The materials after C-ring compression tests were also investigated, with no obvious variation of microstructures were observed for the materials after testing at RT, 345 °C and 650 °C. However, for the materials after testing at 950 °C, some pores were found at the interface, as well as in the Cr coating near the interface, as marked by green arrows in Fig. 3d.

Nanoindentation experiments were performed on the polished cross-sections of the Cr-coated materials in four areas in the form of line scans, as marked in Fig. 3a. Setting interface is the zero point, Area#1 is located in the middle of the coating (−8 μm away from the interface), Area#2 is located in the Cr coating but closer to the coating/substrate interface (−3 μm away from the interface), Area#3 and Area#4 are both located in the substrate (+3 μm and + 8 μm away from the interface, respectively). Results are plotted in Fig. 3e and f, with detailed values of each data point summarised in Table S3 in the Supplementary Materials. Little to no variation of hardness and elastic modulus were found for the as-received materials and materials tested at RT, therefore, only the results of as-received materials were presented in the following text. Overall, the substrate has a lower hardness and modulus value than the coating.

For as-received materials, the middle of the Cr coating layer (Area#1 (−8 μm)) showed a H value of ~4.17 GPa and E of ~247.97 GPa. As one moved towards the coating/substrate interface (Area#2 (−3 μm)), a higher hardness value, H (~5.69 GPa, ~34.6 % higher than Area#1) was measured while the elastic modulus, E (~241.65 GPa) remained similar. In the substrate, the H and E values in Area#3 (+3 μm) and Area#4 (+8 μm) were found to be similar: ~2.51 GPa (H) and 108.43 GPa (E), ~2.58 GPa (H) and 107.55 GPa (E), respectively. Note the data from these two areas overlapped in Fig. 3e and f. This is as expected as PVD method has minimum impact on the underlying substrate.

After testing at 345 °C, 650 °C and 950 °C, the middle of the Cr coating (Area#1 (−8 μm)) showed a general increase in the hardness values compared with as-received materials: ~4.71 GPa at 345 °C (11.8 % increasing), ~4.84 GPa at 650 °C (16.1 % increasing) and ~ 4.78 GPa at 950 °C (14.6 % increasing), Fig. 3e. As for the elastic modulus, it remains constant after testing at 345 °C (~244.72 GPa), a 7.4 % increase after testing at 650 °C and 950 °C (~264.27 GPa and ~ 268.46 GPa, respectively), Fig. 3f. In coating Area#2 (−3 μm away from the interface), the hardness value (after testing at 345 °C) increased to ~6.30 GPa (11.1 % higher than as-received materials), and then decreased to 5.49 GPa (3.5 % lower) and 5.21 GPa (8.4 % lower) after testing at 650 °C and 950 °C, respectively, Fig. 3e.

In both substrate Area#3 (+3 μm) and Area#4 (+8 μm), compared with as-received materials, the H first increases by 12.2 % after testing at 345 °C (~2.84 GPa and ~ 2.79 GPa, respectively), be similar to as-received materials after testing at 650 °C (~2.60 GPa and ~ 2.53 GPa, respectively), and then increases by 12.2 % after testing at 950 °C (both ~2.81 GPa), Fig. 3e. The E values remained constant after testing at all temperatures: 105.77 GPa to 108.43 GPa, Fig. 3f. The potential reason of the variations of local properties of post-tested materials will be discussed in Section 4.

3.2. Load-displacement curves and hoop stresses/strains

For the Cr-coated cladding material, two samples were tested at each temperature (samples S1 and S2 at RT, S3 and S4 at 345 °C, S5 and S6 at 650 °C, S7 and S8 at 950 °C), and their mechanical behaviour was found to be consistent. Consequently, one representative load–displacement curve for the materials tested at each temperature is presented in Fig. 4, and the other load–displacement curves are presented in Fig. S1 in the Supplementary Materials.

At RT, a linear relationship (slope of ~0.02) of load and displacement can be observed at the initial loading stage in the curves (Fig. 4a), which ends at ~0.72 of the peak load (P_U), Fig. 4a. At 345 °C, linear relationship is also observed but with a slope of ~0.005 (25 % of that at RT), and ends at ~0.96P_U. However, at 650 °C and 950 °C, such linear relationship was not observed, which is different from materials tested at RT and 345 °C, Fig. 4b. The potential reasons will be discussed in Section 4.

At RT and 345 °C, the maximum hoop strength calculated from Eq. (4) are summarized in Table 1. Note that, due to the sample deformation exceeding the validity criteria specified in ASTM Standard C1323–16 [23], the calculated strength could be an overestimation. The calculated maximum hoop strength at RT is ~955.5 MPa which is ~4.7 times of that tested at 345 °C (~203.0 MPa). Due to the large deformation of materials tested at 650 °C and 950 °C (Fig. 4b), Eq. (4) cannot be applied. Additionally, as described in Section 2.2.5, *in situ* radiography projections were collected to monitor the coating cracks during the experiments. The loads at which these cracks were first detected by radiography (also confirmed with XCT scans) are summarized in Table 1, and the corresponding hoop stresses are calculated based on Eq. (4); these stresses are referred to as coating failure hoop strength. For instance, at RT, coating cracks were firstly detected at ~0.73P_U, with a corresponding coating failure hoop strength of ~697.5 MPa. At 345 °C, coating cracks were firstly detected at ~0.96P_U, with a corresponding coating failure hoop strength of ~185.5 MPa.

Moreover, the hoop strains when coating cracks first being observed and at peak load were calculated based on the corresponding hoop stress and elastic modulus of the Cr coating (measured by nanoindentation method, Table S3), and summarized in Table 1. At RT, the hoop strains at the first observation of coating cracks and at peak load are 0.28 % and 0.38 %, respectively. Such values are respectively 3.7 times and 4.6 times of that measured at 345 °C: 0.075 % (first coating crack formation) and 0.083 % (peak failure strain). Note that the elastic modulus of the Cr coating may decrease at elevated temperatures, which suggests that the calculated strains at 345 °C could be lower than the actual values.

During each XCT scan period (~5 mins), tested samples were held at a constant displacement. In addition to the sudden decrease of load (load drops), progressive decreasing of load was also observed for materials tested at all temperatures, *i.e.*, load relaxations, are marked in Fig. 4. Such load relaxations were commonly reported for such PVD Cr-coated Zircaloy materials under various loading configurations, *e.g.* Cr-coated Zircaloy-4 claddings under C-ring compression at RT and 345 °C reported by Yuan et al. [4], and Cr-coated Zircaloy-4 sheet specimens under RT tensile tests reported by Nguyen et al. [32]. While a comprehensive analysis of these load relaxations is beyond the scope of current study, and the load relaxation values are tabulated in Table S4.

3.3. Failure processes and crack patterns at different temperatures

In this section, real-time XCT scans were analysed to investigate the failure processes of the materials tested at different temperatures, with representative 2D XCT slices of X-Y plane and 3D visualisation of cracks presented in Fig. 5, Fig. 7, Fig. 9 and Fig. 11. In these figures, the XCT slices are collected at same locations of the tested materials at different loading steps for direct comparison. The average distance between coating cracks was measured using ~80 XCT slices (of the X-Y plane) collected across the width of each sample. SEM images are collected to

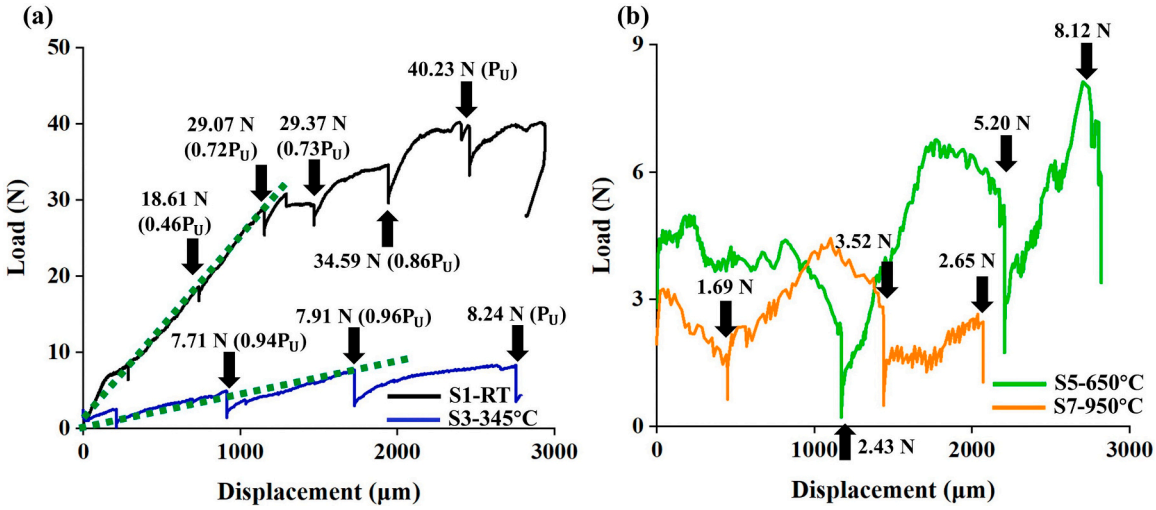

Fig. 4. Representative load–displacement curves of the C-ring compression tests of the materials at elevated temperatures: (a) sample S1 tested at RT and sample S3 tested at 345 °C; (b) sample S5 tested at 650 °C and sample S7 tested at 950 °C. The arrows indicate where the XCT scans were collected, as well as the load relaxations of the tested C-ring samples during the XCT scanning period. The dashed lines marked in Fig. 5a represent the linear relationship of load and displacement of the materials at the initial loading stage in the curves.

Table 1
The width of specimens, the load, corresponding hoop stresses, and strains at first coating crack(s) formation, peak loads and calculated maximum hoop stresses for Cr-coated cladding materials tested at both RT and 345 °C.

Specimen	Sample width (mm)	Load (N) and corresponding hoop stress (MPa) and strain at first coating crack	Peak load (N)	Maximum hoop stress (MPa) and strain
S1-RT	2.5 ± 0.1	29.4 /719.6 /0.29 %	40.2	985.8/0.40 %
S2-RT	2.4 ± 0.1	28.5 /675.0 /0.27 %	39.1	924.6/0.37 %
S3–345 °C	2.5 ± 0.1	7.7 /192.8 /0.078 %	8.2	205.2/0.084 %
S4–345 °C	2.4 ± 0.1	7.0 /178.4 /0.073 %	7.8	201.2/0.082 %

investigate the crack patterns of post-tested materials. At each testing temperature, the samples showed similar failure process and crack patterns, therefore one specimen is selected as representative example: sample S1 at RT, sample S3 at 345 °C, sample S5 at 650 °C and sample S7 at 950 °C.

3.3.1. *Cladding materials tested at RT*

For sample S1 at RT, the simultaneous formation of multiple coating cracks was captured at 0.73P_U (29.4 N; estimated hoop stress: 719.6 MPa; estimated hoop strain: 0.29 %), Fig. 5a. Three typical examples of the cracks (Crack#1 to Crack#3) are selected and reconstructed in 3D as representative examples to illustrate the failure process, Fig. 5a.

Fig. 5b shows the 3D visualisation of Crack#1 to Crack#3. Once formed, these cracks travelled through the thickness of the Cr coating and arrested at the coating/substrate interface. All the coating cracks formed almost perpendicular to the hoop direction (Y direction). Furthermore, some cracks propagated across the full width of the tested sample (see Crack#1 and Crack#2), while others terminated in the coating, *e.g.*, Crack#3 in Fig. 5b. The average distance between coating cracks was measured to be 89.8 ± 27.1 μm.

With loading to 0.86 P_U (34.6 N; 847.8 MPa; 0.34 %), the number of coating cracks increased, and average distance between coating cracks reduced to 61.3 ± 17.3 μm. For example, in the magnified image in Fig. 5c, the formation of new cracks Crack#4 and Crack#5 was observed in-between the cracks formed in the previous loading step (0.73 P_U in Fig. 5a). With loading to peak load, P_U (40.2 N; 985.8 MPa; 0.40 %), the number of coating cracks further increased (*e.g.* a newly formed Crack#6 is shown in the magnified image in Fig. 5d). Note that Cracks#1 to #3 (in Fig. 5a and b) are the same cracks in Fig. 5c to e. 3D visualisation shows none of the coating cracks propagated into the underlying substrate, Fig. 5e. Crack#4 terminated in the coating (Fig. 5e), and crack bridging was observed (marked by open circle in Fig. 5e). The average distance between the coating cracks is measured to be 36.1 ± 9.8 μm.

Coating crack patterns of the materials after testing at RT are presented in Fig. 6. On the coating surface, cracks propagated almost perpendicular to the hoop loading direction (Fig. 6a, an angle range of 88° to 91°), shows consistency with the findings from XCT imaging. Width of cracks (marked by yellow arrows in Fig. 6b) was measured to be 1 to 4 μm. These cracks propagated mostly in an intergranular mode on the surface of the coating (deflected along the Cr grain boundaries), Fig. 6b.

3.3.2. *Cladding materials tested at 345 °C*

For Sample S3 tested at 345 °C, simultaneous formation of four coating cracks was firstly observed at 0.94 P_U (7.7 N; 192.8 MPa; 0.078 %), Fig. 7a. 3D visualisation of a typical crack, Crack#3, showed it arrested at the coating/substrate interface and travelled across the width of the C-ring sample once formed. Crack bridging was also found, Fig. 7b. Coating cracks imaged by XCT all propagated at an angle range of 81° to 96° with respect to the loading line direction (Fig. 7b), and average distance between coating cracks was measured to be 367.5 ± 160.0 μm.

With the load being increased to P_U (8.2 N; 205.2 MPa; 0.084 %), more coating cracks formed, *e.g.*, newly formed Crack#5 and Crack#6 were shown in the magnified image in Fig. 7c. Note that Crack#3 (in Fig. 7a and b) is the same crack in Fig. 7c and d. Crack#5 was found to have terminated in the coating, while Crack#6 propagated across the width of the sample, Fig. 7d. Average distance between coating cracks reduced to 112.9 ± 49.1 μm.

Coating crack patterns are presented in Fig. 8. Cracks travelled in a range of 81° to 96° against the hoop direction (Fig. 8a, consistent with the observations from XCT). Such angle range is larger than that at RT. Similar to the RT test, the coating cracks at 345 °C also propagated almost in an intergranular mode, Fig. 8b. But a larger opening of the coating crack at the coating surface was found at 345 °C (width of coating cracks is between 1 and 8 μm).

3.3.3. *Cladding materials tested at 650 °C*

For the sample S5 tested at 650 °C, simultaneous formation of three

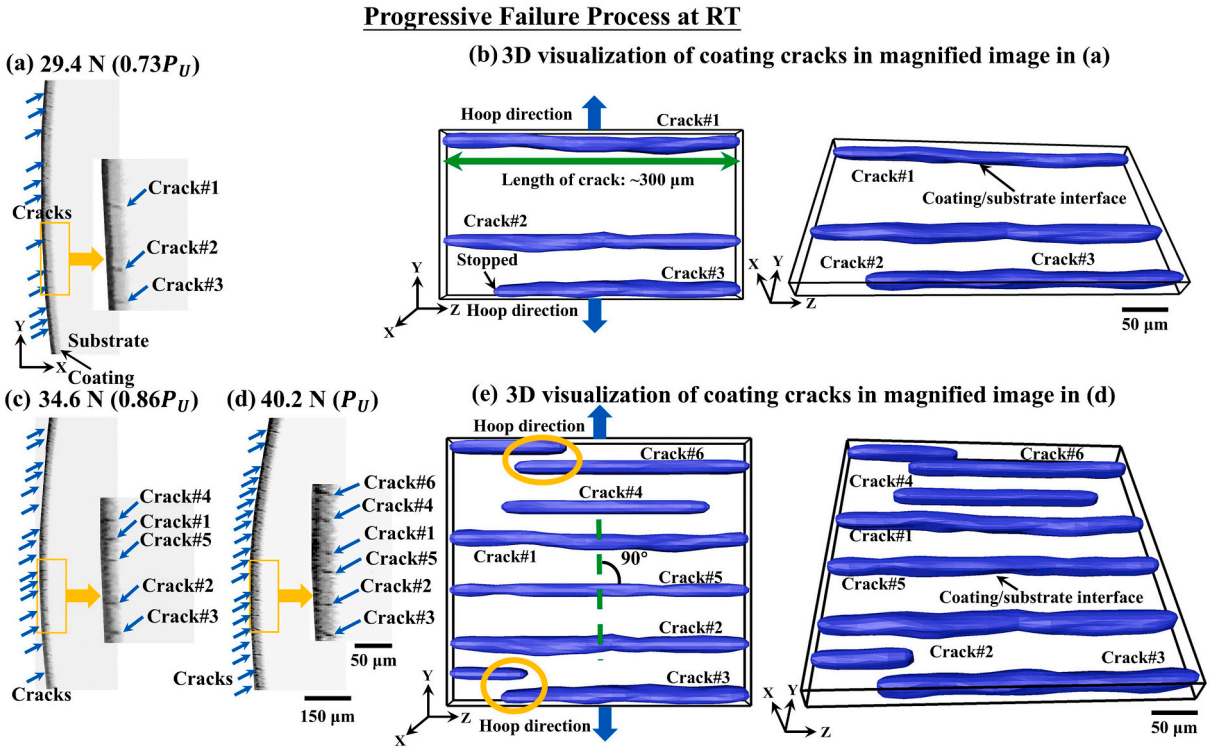

Fig. 5. Failure process of the cladding material tested at RT, illustrated from sample S1. (a), (c) and (d) are *in situ* XCT slices of X-Y plane, and the magnified images extracted from the same location in the materials at increasing loading stages. (b) and (e) are 3D visualisation of part of the coating cracks, the selected length in (b) and (e) is ~300 μm (marked by green arrows in Fig. 5d), ~12 % of the total width of the sample: ~2.5 mm. (a) Scan at 29.4 N (0.73P_U), (b) visualisation of cracks in magnified images in (a), (c) scan at 34.6 N (0.86P_U), (d) scan at 40.2 N (P_U), and (e) visualisation of cracks in magnified images in (e). Coating cracks were found perpendicular to hoop direction, as marked in Fig. 5b and e.

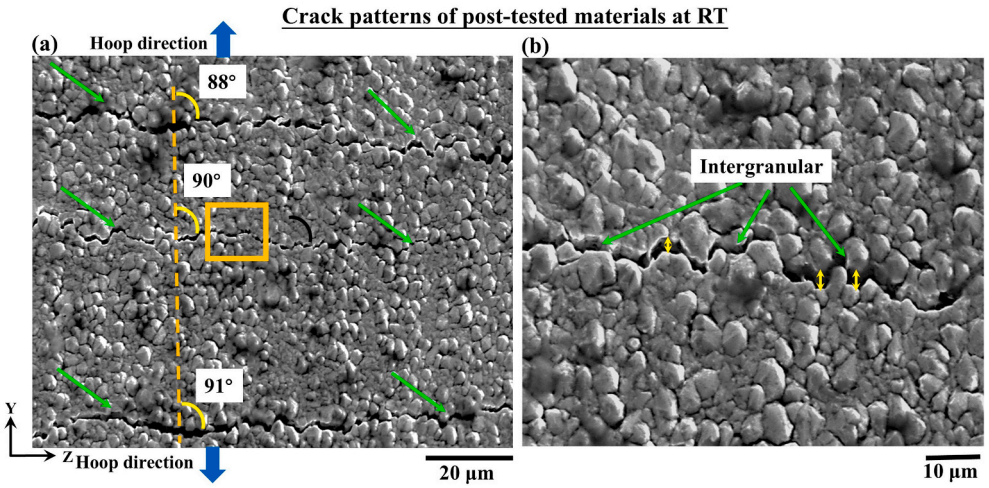

Fig. 6. SEM images (SE2 mode) collected at the outer surface of the sample show the coating crack patterns at RT, illustrated by sample S1: (a) low magnification view shows coating cracks (marked by green arrows), angles of coating cracks against the hoop direction were also marked.; (b) high magnification view (collection area was marked by open rectangle in Fig. 6a) shows coating cracks propagated in an intergranular mode. Width of coating cracks is marked by yellow arrows in Fig. 6b.

coating cracks was observed at 5.2 N based on the XCT scan, Fig. 9a. 3D visualisation of a representative crack, Crack#1, showed it propagated perpendicular to the hoop direction, and arrested at the coating/substrate interface, Fig. 9b. The width of Crack#1 on the coating surface is ~8 μm, and the average distance between coating cracks is estimated to be 342.9 ± 201.7 μm.

Note that Cracks#1 to #3 (in Fig. 9a and b) are the same cracks in Fig. 9c and d. Different from RT and 345 °C, no newly formed cracks were observed upon further loading until the peak load at 8.1 N, Fig. 9c. Moreover, 3D visualisation revealed these coating cracks propagated into the underlying substrate to a depth of ~10 μm, Fig. 9d. On the surface of the coating, the opening of coating cracks further increased to ~20 μm, Fig. 9d.

SEM images of the surface coating crack patterns of the materials after testing at 650 °C are presented in Fig. 10. The primary coating cracks travelled mostly perpendicular to the hoop direction (Fig. 10a),

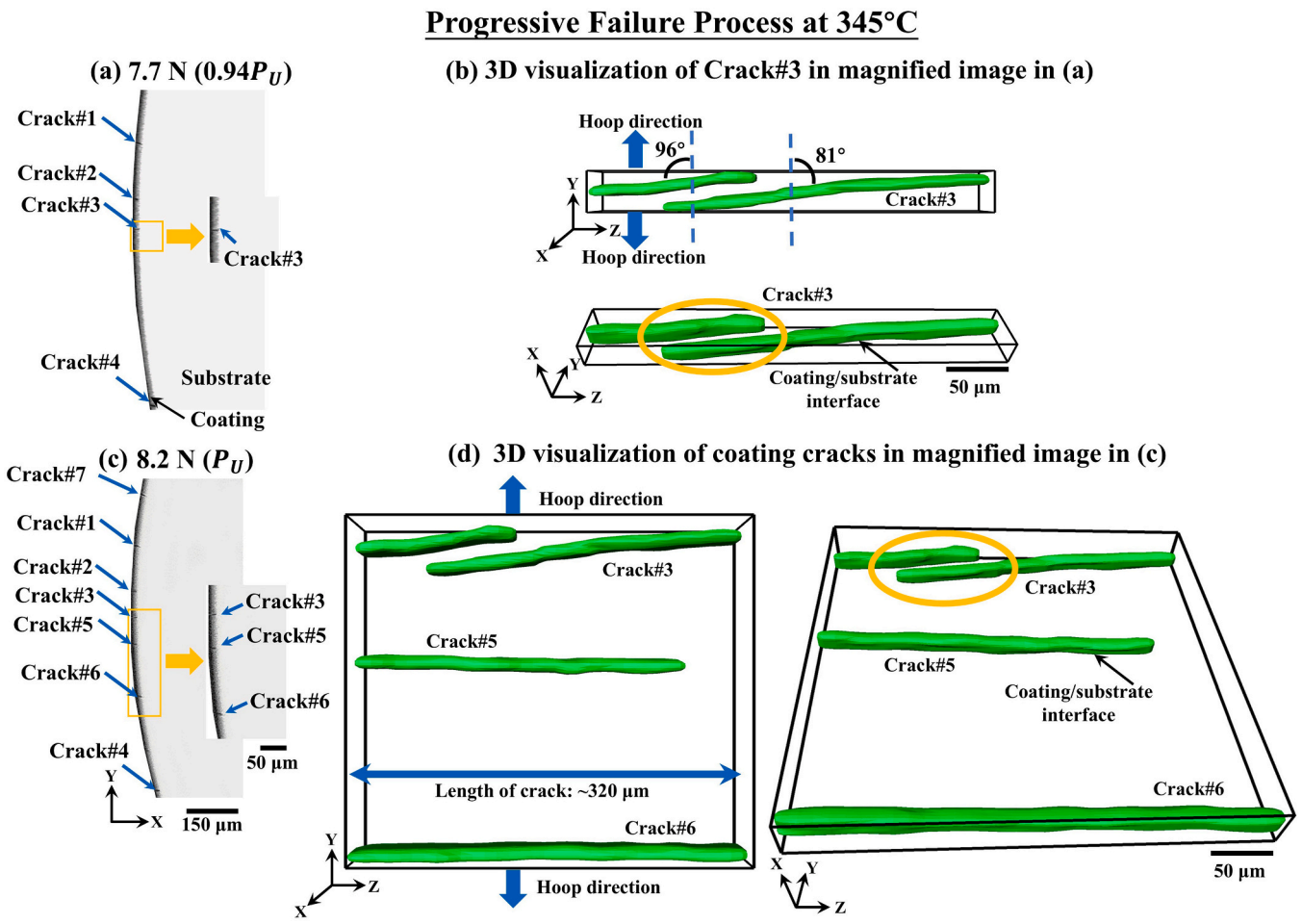

Fig. 7. Failure process of the cladding material tested at 345 °C, illustrated from sample S3. (a) and (c) are *in situ* XCT slices of X-Y plane, and the magnified images extracted from the same location in the materials at increasing loading steps. (b) and (d) are 3D visualisation of part of the coating cracks, the selected length in (b) and (d) is ~320 μm (marked by arrows in Fig. 7d), ~13 % of the total width of the sample: ~2.5 mm. (a). (a) Scan at 7.7 N (0.94P_U), (b) visualisation of Crack#3 in magnified images in (a), (c) scan at 8.2 N (P_U), (d) visualisation of cracks in magnified images in (d). Angles of coating cracks against the hoop direction were marked in Fig. 7b.

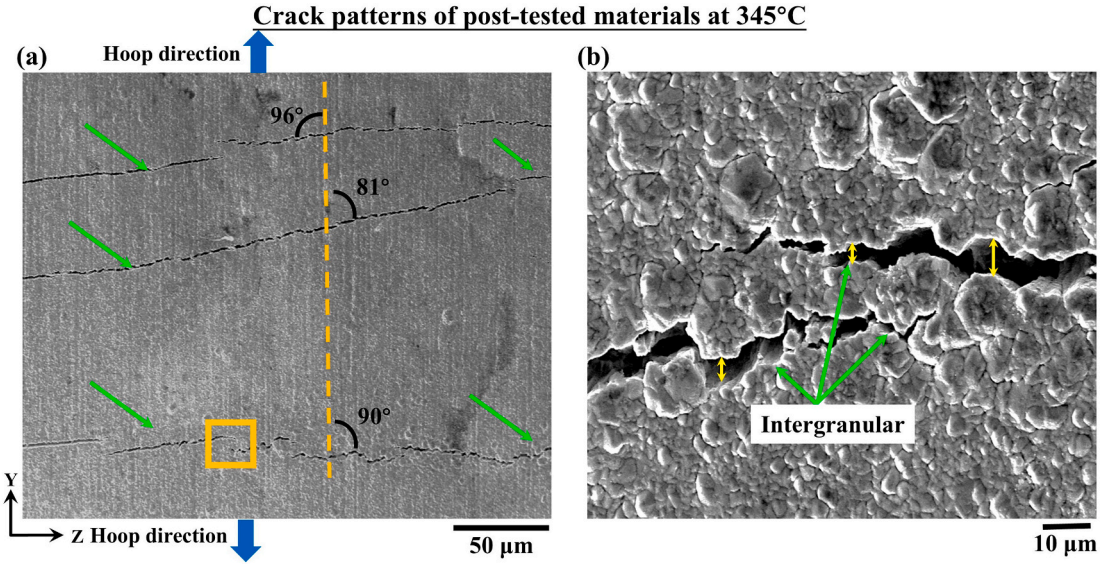

Fig. 8. SEM images (SE2 mode) collected at the outer surface of the sample show the crack patterns of material after testing at 345 °C, illustrated by sample S3: (a) low magnification view shows coating cracks (marked by green arrows); angles of cracks against the hoop direction were also marked. (b) high magnification view (collection area was marked by open rectangle in Fig. 8a) shows coating cracks propagated in an intergranular mode. Width of coating cracks is marked by yellow arrows in Fig. 8b.

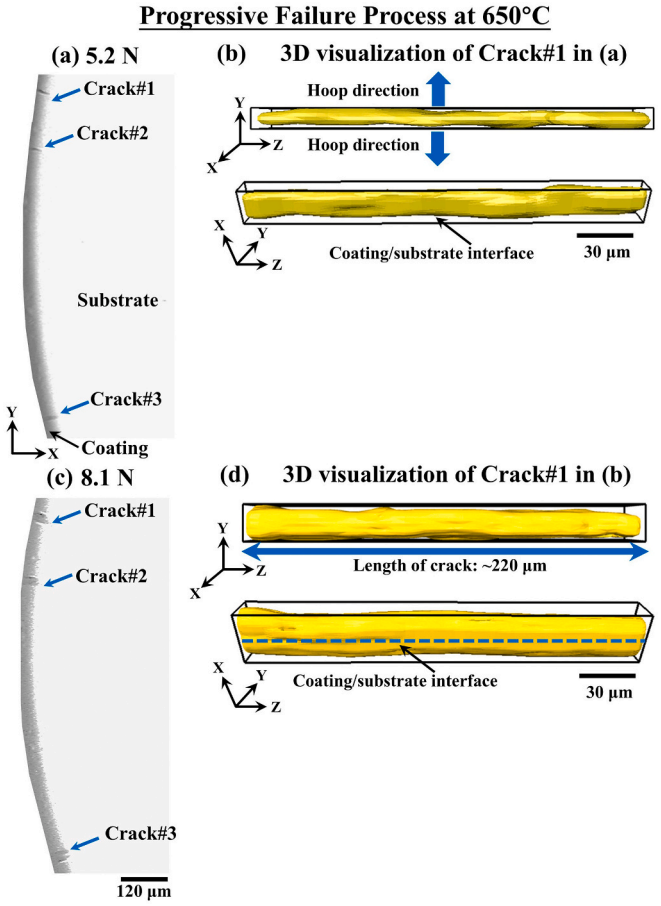

Fig. 9. Failure process of the cladding material tested at 650 °C, illustrated from sample S4. (a) and (c) are *in situ* XCT slices of X-Y plane collected at increasing loading stages. (b) and (d) are 3D visualisation of Crack#1, with selected length is ~220 μm, ~9 % of the total width of the sample: ~2.4 mm. (a) scan at 5.2 N, (b) visualisation of Crack#1 in magnified image in (a), (c) scan at 8.1 N, and (d) visualisation of Crack#1 in magnified image in (b).

which is consistent with the observations from XCT imaging. Between these primary coating cracks, some finer cracks can be found in an intergranular mode, Fig. 10b. However, these finer cracks have a width less than 3 μm, which is below the detection resolution (3.25 μm/pixel) of both XCT imaging.

3.3.4. *Cladding materials tested at 950 °C*

For sample S7 tested at 950 °C, simultaneous formation of multiple coating cracks was observed at 3.5 N, Fig. 11a. Two typical examples of the cracks (Crack#1 and Crack#2) are selected to illustrate the failure process, as marked in the magnified image in Fig. 11a. The coating cracks arrested at the coating/substrate interface, Fig. 11b. Some cracks propagated across the width of sample (Crack#2 in Fig. 11b), while others terminated in the coating, see Crack#1 in Fig. 11b. The average distance between these cracks is measured to be 231.7 ± 119.2 μm. The total number of coating cracks increased with further loading, with the last XCT scan collected at 2.7 N, Fig. 12c. Newly formed Crack#3 and Crack#4 were observed in the magnified image, Fig. 12c. Note that, Crack#1 and Crack#2 (in Fig. 11a and b) are the same cracks in Fig. 11c and e. Under the current resolution of XCT images (pixel size of 3.25 × 3.25 μm), coating cracks were observed to remain arrested at the interface, Fig. 12d. Distance between the coating cracks reduced to 83.7 ± 23.4 μm.

Coating crack patterns of sample S7 after testing at 950 °C are presented in Fig. 12. Cracks formed in an angle range of 89° to 92° against the hoop direction (Fig. 12a, consistent with the observations from XCT), which is similar to that at RT. However, different from the cracks formed at RT and 345 °C, transgranular failure mode was found at the crack tips at 950 °C, Fig. 12b. Width of the coating crack on the surface of sample is measured to be 1 to 6 μm.

To summarize, different failure processes and coating crack patterns were observed for the material tested at different temperatures. At RT, 345 °C and 950 °C, the number of coating cracks increased with increasing load. At these three testing temperatures, coating cracks arrested at the coating/substrate interface. However, at 650 °C, the increasing of load did not lead to the increase in the number of coating cracks, but resulted in the further opening of these cracks and drove the cracks deeper into the underlying substrate.

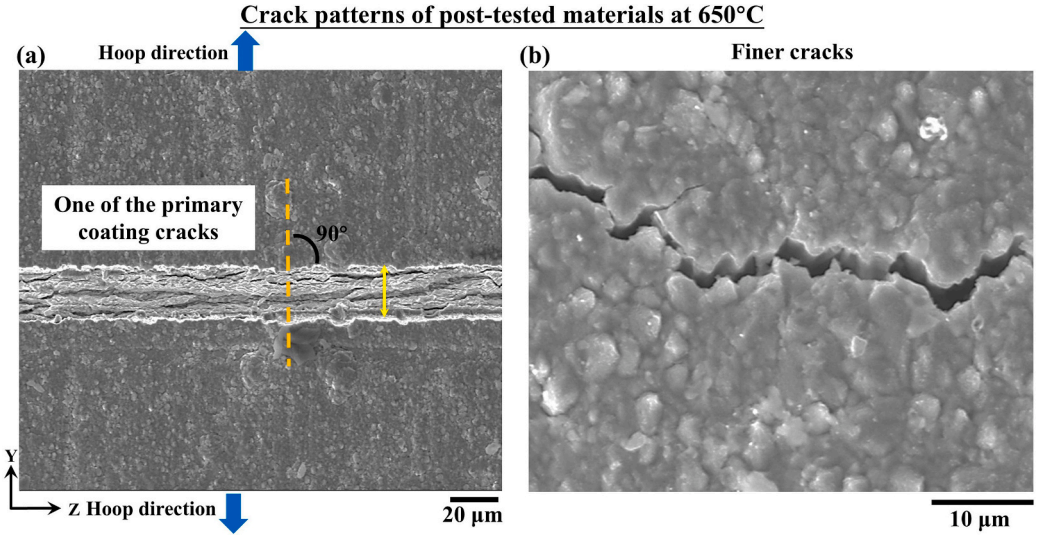

Fig. 10. SEM images (SE2 mode) collected at the outer surface of the sample show the crack patterns of material after testing at 650 °C, illustrated by sample S5: (a) low magnification view shows one of the primary coating cracks, Width of coating cracks is marked by yellow arrows. (b) high magnification view showing finer cracks between these primary coating cracks.

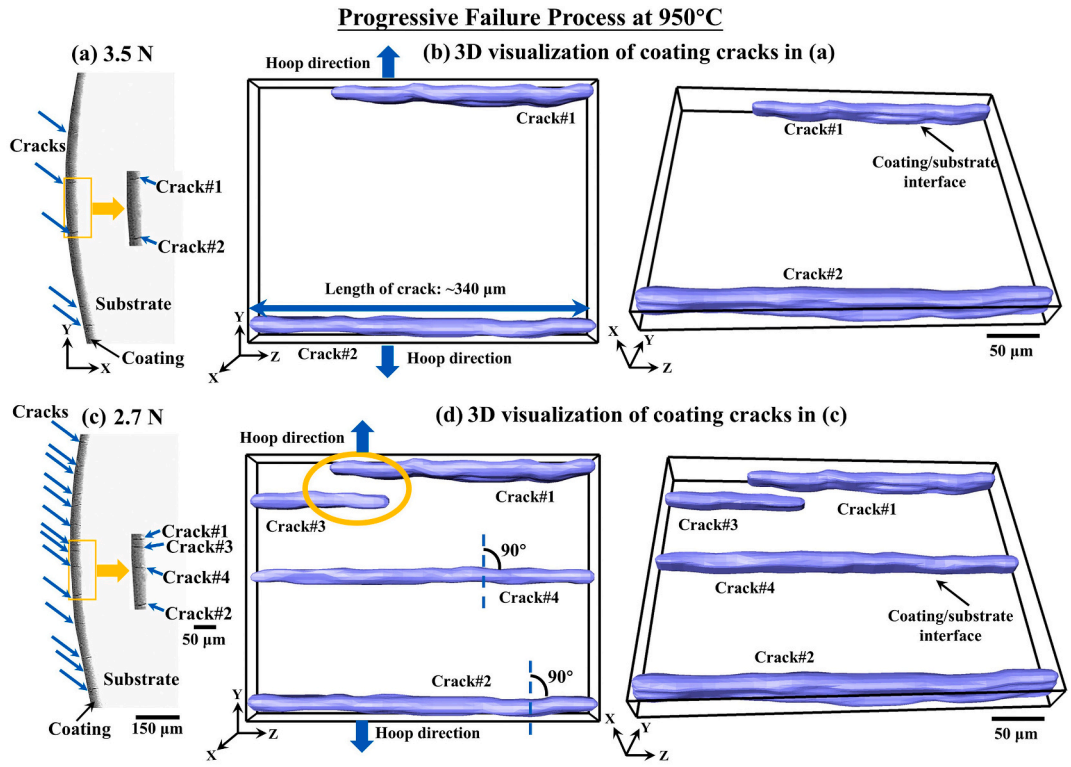

Fig. 11. Failure process of the cladding material tested at 950 °C, illustrated from sample S7. (a) and (c) are *in situ* XCT slices of X-Y plane, and the magnified images extracted from the same location in the materials at increasing loading steps. (b) and (d) are 3D visualisation of part of the coating cracks, the selected length in (b) and (d) is ~340 μm, ~15 % of the total width of the sample: ~2.3 mm. (a) Scan at 3.5 N, (b) visualisation of cracks in magnified images in (a), (c) scan at 2.7 N, (d) visualisation of cracks in magnified images in (d). Angles of coating cracks against the hoop direction were marked in Fig. 11b.

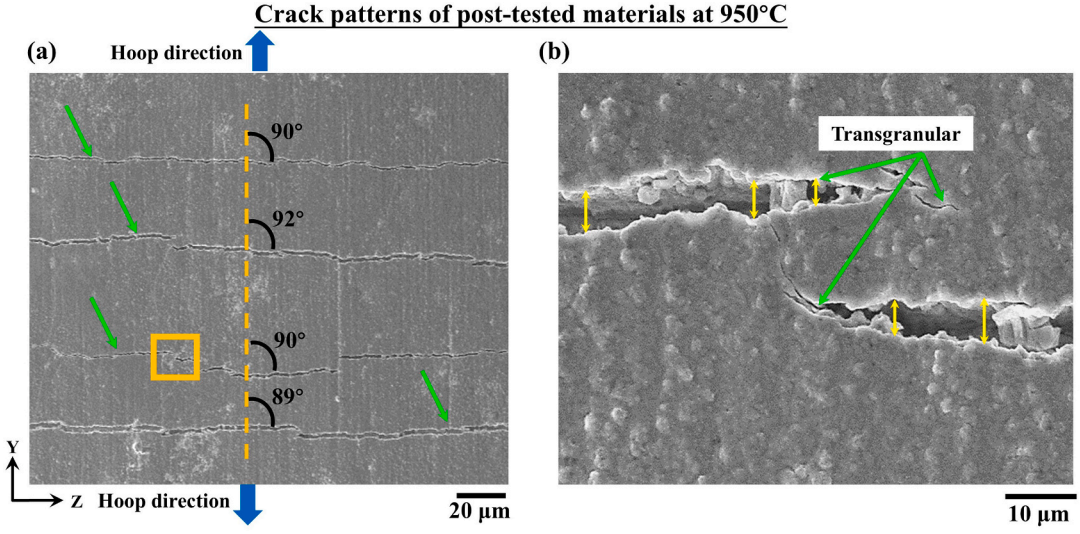

Fig. 12. SEM images (SE2 mode) collected at the outer surface of the sample show the crack patterns of material after testing at 950 °C, illustrated by sample S7: (a) low magnification view shows coating cracks (marked by green arrows), angles of coating cracks against the hoop direction were also marked.; (b) high magnification view (collection area was marked by open rectangle in Fig. 12a) shows crack patterns. Width of coating cracks is marked by yellow arrows in Fig. 12b.

4. Discussion

4.1. Microstructures of PVD Cr-coated materials after high-temperature testing

No obvious pores were found at the coating/substrate interface in the as-received materials, consistent with findings of similar PVD Cr-coated Zircaloy from open literature [4,33]. However, circular isolated voids in the coating were formed close to the interface area after testing at 950 °C (Fig. 3). This could be attributed to two primary mechanisms: (i) interdiffusion of Cr into Opt. ZIRLO™ substrate; and (ii) recrystallisation of Cr grains under high temperature testing (1 h testing duration).

When heated to the same temperature, the diffusion coefficient of Cr diffusing into Zr is greatly higher than Zr into Cr. For instance, in the temperature range of 748 °C to 1197 °C, the diffusion coefficient of Cr into Zr is between 8.7×10^{-13} and 5.5×10^{-12} m^2/s [34], which is more

than 1000 times higher than the diffusion coefficient from Zr into Cr (10^{-15} to 10^{-16} m^2/s) [35]. Moreover, at the same temperature, maximum solubility of Cr in Zr is higher than Zr in Cr [36]. For instance, at 1300 °C, the maximum solubility of Cr in Zr is ~8 at.%, and it is significantly higher than Zr in Cr which is ~0.6 at.% [37,38]. These all result in asymmetric atomic diffusion at the coating/substrate interface region at high temperatures as Cr atoms diffuse more into the Zr substrate, and higher diffusion flux of vacancies diffuse from Zr to Cr [39]. The clustering and coalescence of these vacancies can result in micro-size pores in the Cr coating. However, the diffusion coefficient of Cr into Zr at RT is reported to be ~3.6×10^{-19} m^2/s [34]: around 10^{-6} of that at 748 °C to 1197 °C. This indicates that such asymmetric atomic diffusion at low temperatures (and therefore interdiffusion or pore formation driven by diffusion) can be effectively suppressed which is consistent with the observation of current work.

As reported by Li et al. [36], they annealed their PVD Cr-coated (~0.5 μm of coating thickness) Zircaloy-4 materials at 200 to 600 °C in high vacuum furnace for 60 mins (similar to the high temperature duration in current work which is about 1 h), and used transmission electron microscopy (TEM) to investigate the microstructural evolution of the Cr coating. At 600 °C, the recrystallisation of PVD Cr grains results in the variation of finer Cr grains at the interface region from irregular shapes into columnar structures, and consequently causes the formation of nano-sized cavities at the interface region. Subsequently, these nano-sized cavities coalesced together and formed micro-size pores [40] at the coating/substrate interface area. Furthermore, Li et al. [36] also reported the broadening of column Cr grains (in the middle of Cr coating) with increasing of annealing temperature: from 30 nm after annealed at 200 °C for 1 h to 68 nm after annealed at 600 °C for one hour [36]. This could also result in variation of local properties of the Cr coating, as discussed in Section 4.2.

Moreover, as reported by Fazi et al. [41], interdiffusion of Cr and Zr elements could occur at the interface area at high temperatures, and consequently generate an intermixed bonding region and brittle intermetallic (*e.g.*, $ZrCr_2$) at the interface area. These intermetallic phases are brittle and susceptible to crack initiation, and could potentially act as stress concentrators, thereby compromising the strength of the entire cladding system. In future work, advanced characterisation techniques such as transmission electron microscopy (TEM) will be employed to analyse interdiffusion zones and to identify any intermetallic compounds formed at the coating/substrate interface.

4.2. Local properties of PVD Cr-coated materials after high-temperature testing

The hardness (~4.17 GPa) and elastic modulus (~247.9 GPa) measured in the middle of Cr coating (Area#1) in as-received materials are consistent with similar PVD Cr coating from open literature: 3.8 GPa to 8.7 GPa of *H* [4,16,21,33,42,43], and 227.5 GPa to 328.8 GPa of *E* [4,16,21,33,42]. The differences in the coating local properties could be caused by the different manufacturing parameters (*e.g.*, pressure and temperature of the gas [44]). Detailed information of these coatings and local properties are reviewed and summarized in Table S5 in the Supplementary Materials. Moreover, in current work, the hardness of coating Area#2 (close to the interface) is 34.6 % higher than that in Area#1. This is attributed to smaller size of Cr grains clustered near the interface (Area#2, Fig. 3) compared to the larger column Cr grains in Area#1 [4]. The lower hardness (~2.51 GPa) and elastic modulus (~108.43 GPa) of ZIRLO substrate indicates substrate is more ductile than the coating.

For the materials after high temperature testing, increasing in hardness and elastic modulus in Area#1 were found. As discussed in Section 4.1, one potential reason is the microstructural variation in the columnar Cr grains at elevated temperatures [36]. Another potential reason is the variation of residual stress in the PVD Cr coating at high temperatures. Quillin et al. [21] reported 300 MPa tensile residual stress in their PVD Cr coating (~5.3 μm of coating thickness), which relaxed at elevated temperatures due to recrystallisation of Cr grains [36]. The observed variation in local properties in Area#1 (middle of the Cr coating) may thus result from combined effects of microstructural evolution and residual stress relaxation. Future work is needed to identify grain size variations and residual stress relaxation in the coating [45].

In coating Area#2 (close to the interface), the hardness increased to 6.3 GPa after tested at 345 °C. It is widely reported that under PVD process, at the interface area, the Cr atoms build up in a disordered manner and form amorphous Cr [40]. Under annealing at high temperatures, such amorphous Cr could transform into crystalline Cr [36]. Additionally, Hoshino et al. [46] reported the recrystallisation of their electrodeposited amorphous Cr coating (~20 μm of coating thickness) occurred when annealed at 300 °C to 400 °C, evidenced by the Cr peaks in their X-ray diffraction measurements. Furthermore, for their as-received amorphous Cr coating, the Vicker's hardness was measured to be 1000 Hv, which increased to 1200 Hv after annealed at 300 °C, and 1500 Hv after annealed at 400 °C [46]. These all indicate that, in current work, the transition of amorphous Cr into crystalline Cr at the interface region could occur at 345 °C, and consequently resulted in the increase in measured hardness values. With further increase in temperature, the finer Cr grains at the interface region coalesced and transitioned from irregular shapes into columnar structures [36]. This could cause the steady decreasing of hardness in coating Area#2 in current work with further increasing of temperature. Future EBSD mapping at the interface area will be conducted to quantitatively investigate the variation of Cr grains at elevated temperatures.

The hardness of substrate increased by 12.2 % after tested at 345 °C but remained unchanged after tested at 650 °C. Yi et al. [47] reported similar trend in their ZIRLO®, with the Vicker's hardness increased from 260 Hv (as-received) to 280 Hv after annealed at 300 °C for 60 mins, and then reduced to 260 Hv after annealed at 400 °C for 60 mins. They suggested this could be caused by the precipitate of Nb from the substrate; with further increasing of temperature, recovery processes may occur, potentially mitigating the impact of the Nb precipitation on hardness [47]. Moreover, as suggested by Jiang et al. [48], for the Zircaloy materials being annealed below 700 °C, the coalescence of α-grain could reduce its hardness. For the materials tested at 950 °C, the increased hardness could be caused by the refinement of the equiaxed α-grain. As reported by Song et al. [49], when the annealing temperature of Zircaloy-4 materials is higher than 1000 °C, the atomic diffusion ability and its precipitation are enhanced, which consequently full recrystallisation and dispersion of refined equiaxed α-grain. Future work using EBSD and energy dispersive X-ray spectroscopy (EDX) mapping of the coating cross-sections will be carried out for thorough analysis.

4.3. Mechanical behaviour and coating failure strain/stress

The linear relationship in the load-displacement curves at RT and 345 °C (Fig. 4a) could be attributed to the initial elastic deformation of the materials. This has been commonly reported in similar materials under different testing configurations [32], *e.g.*, PVD (~14.4 μm in thickness) Cr-coated Zircaloy-4 cladding tubes under C-ring compression tests at RT and 345 °C [4]. However, the linear relationship was not observed at 650 °C and 950 °C, Fig. 4a, where significant softening of the material was observed, which is the inherent physical properties of metallic materials. The softening of Zircaloy materials at elevated temperatures was commonly reported, especially when tested above 600 °C [50].

The failure hoop strain/stress of the coating is defined as the strain/stress at which the first coating cracks were formed. They are 0.28 %/~697.5 MPa at RT, and 0.075 %/~185.5 MPa at 345 °C. For the Zircaloy claddings in LWRs, the designed failure hoop strain is reported to be 0.1 % to 0.3 % [51], and the designed failure hoop strain/stress under normal operating condition (~345 °C) is 1 % to 2 % and 90 MPa to 120 MPa [52–54]. The failure hoop strain of Cr coating at RT in this

work is in the reported range, and the failure hoop stress of Cr coating is beyond such range, indicating competitive mechanical behaviour of current Cr-coated materials at servicing conditions in LWRs. As mentioned in Section 3.2, the actual coating failure strain at 345 °C is likely much higher than the calculated value. To obtain more precise hoop strain measurements at elevated temperatures, future research will incorporate high-temperature nanoindentation measurements to determine the actual elastic modulus of the Cr coating at elevated temperatures.

Very limited coating failure hoop strain/stress values of Cr-coated Zircaloy cladding materials were reported from open literature, as summarised in Table S5 in the Supplementary Materials. For instance, Yuan et al. [4] reported coating failure hoop strain/stress of their PVD Cr-coated Zircaloy-4 materials under same testing condition: 0.34 %/~897 MPa at RT and ~510 MPa at 345 °C. In this work, the coating failure strengths are 22.2 % and 63.6 % lower at RT and 345 °C [4], respectively, as well as 17.6 % lower of coating failure strain at RT. The variation of microstructures could result in variation of local properties in Cr coatings, and consequently caused the variation of coating failure strain/stress. Specifically, their Cr coating [4] has higher hardness and elastic modulus than that in current work (4.5 GPa *vs.* 4.2 GPa and 266 GPa *vs.* 248 GPa), caused by the finer Cr grains in their coating (average area of the Cr grains measured by EBSD mapping is 0.39 ± 1.22 μm^2 *vs.* 1.08 ± 0.80 μm^2 in current work). According to the Hall–Petch relationship [55], a reduced grain size increases hardness and yield strength of the material, and increased elastic modulus improves the material's resistance to elastic deformation. These factors could result in higher coating failure stress/strain in the materials reported by Yuan et al. [4]. Another potential reason is the differences in residual stresses in different Cr coatings. It is widely reported that compressive residual stresses were introduced to the PVD coating during the manufacturing process [21,56,57]. As suggested by Lille et al. [57], higher compressive residual stresses in the coating could result in impeding dislocation motion and reducing the propagation of microcracks. This enhances the coating hardness and delays the fracture initiation in the coating, and consequently increases the coating failure stress/strain. Therefore, the coating failure stress/strain in this work could be affected by the combination of microstructures and residual stresses.

4.4. Failure processes and coating crack patterns

The crack resistance of Cr coatings can be effectively evaluated by monitoring the evolution of surface cracks, particularly through quantifying the number of coating cracks under loading [12]. As discussed in Section 4.2, for the as-received material, the substrate is more ductile than the Cr coating. It has been widely reported that in systems characterised by a brittle coating on a ductile substrate, the formation and progression of coating cracks generally follow three distinct stages: (i) initiation stage where cracks form under relatively low strain; (ii) propagation stage during which the number of cracks increases; and (iii) saturation stage where the number of cracks stabilises, and the initiation of new cracks becomes significantly more difficult [58,59]. However, for a ductile coating on ductile substrate, the formation and progression of coating cracks also follow three stages: (i) initiation stage where coating cracks form under relatively higher strain; (ii) propagation stage with the number of coating cracks is hard to increase, but width of cracks increases; (iii) saturation stage where the width of coating cracks does not increase with further loading as the cracks tend to propagate into the underlying substrate [13,60].

In current work, simultaneous formation of multiple coating cracks at RT occurred at 0.73 P_U, the distance between coating cracks at peak load is: 36.1 ± 9.8 μm (Fig. 13a). Cracks formed almost perpendicular to the hoop direction (88° to 91°). However, crack behaviour is different at 345 °C in three main points: (i) distance between coating cracks at peak load is higher (112.9 ± 49.1 μm (Fig. 13b)); (ii) larger angle range of coating cracks against hoop direction was found (81° to 96°); (iii) cracks opened up further on the coating surface, with width of crack of 1–8 μm against 1–5 μm at RT. This indicates that at RT when the brittle Cr coating subjected to hoop stress, it exhibits a crack formation pattern that follows well-defined, energetically favourable paths, predominantly oriented perpendicular to the hoop direction [4,58,59]. This behaviour is attributed to the coating's limited plasticity at RT, which constrains stress redistribution, thereby leading to a high density of uniformly aligned cracks. In contrast, at 345 °C, the increasing of atomic mobility could enhance the ductility of Cr coating, which consequently results in larger crack width and a reduced crack density at peak load [4,60]. Moreover, as suggested by Xu *et al* [61], the relaxation of compressive residual stress in Cr coating at high temperatures could alter the stress field in the Cr coating. And, the interaction between residual stress relief and applied mechanical loading creates a complex stress state in the coating, consequently deviating crack pathways from hoop direction [62,63]. Additionally, as suggested by Yuan *et al* [4], the thermal expansion mismatch between Cr coating (4.9 to 8.2 × 10^{-6}/°C [64,65]) and the substrate (6.6 × 10^{-6}/°C [66,67]) at elevated temperatures could also generate thermal stresses deviating from hoop direction, and caused the deviation of crack pathways from hoop tensile direction. Therefore, the different crack orientation angles could be caused by the combination effect of residual stress relaxation in the

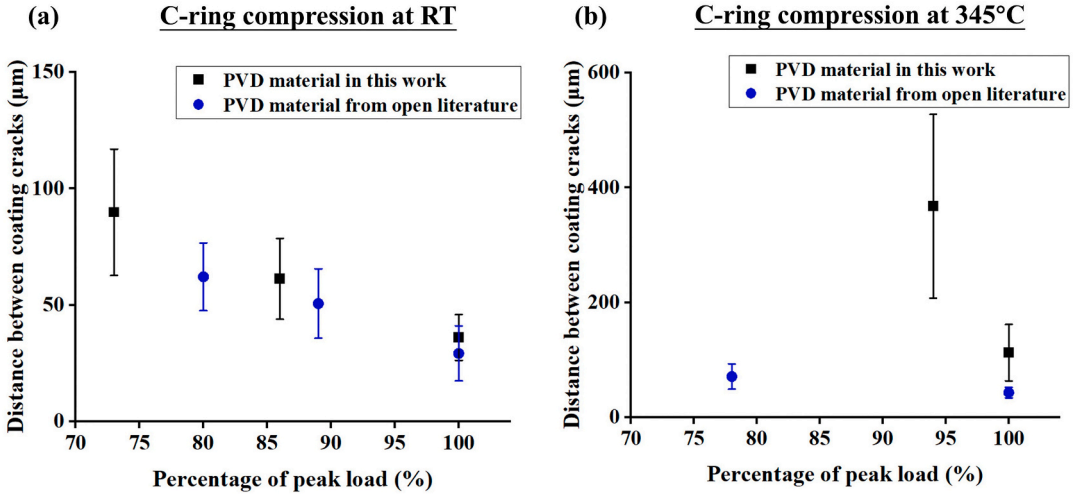

Fig. 13. Distance between the coating cracks measured by real-time XCT imaging at increasing loading stages for PVD Cr-coated materials in current work, and from ref. [4] under same C-ring testing conditions. (a) at RT, and (b) at 345 °C.

coating and thermal expansion mismatch between coating and substrate.

In summary, a brittle failure mode was observed in the PVD Cr-coated materials tested at both RT and 345 °C. The failure processes can be classified into three stages: (i) initial deformation without formation of coating cracks; (ii) simultaneous formation of multiple coating cracks, where lower number of cracks formed at peak load at 345 °C; (iii) the number of coating crack increases with increasing of load, until reaches to saturation at peak load; cracks open up further after peak load but no formation of new cracks.

Moreover, Yuan et al. [4] reported the failure processes and crack patterns of their PVD Cr-coated Zircaloy-4 materials under same testing condition, with the distance between coating cracks also plotted in Fig. 13. Compared with the materials in this work, the distances between coating cracks at their formation, and peak load of their materials are both lower (Fig. 13). This could be attributed to the more brittle of Cr coating in their material (higher hardness and elastic modulus, as discussed in Section 4.2). As suggested by Quillin et al. [62], a more brittle coating exhibits limited plastic deformation capacity inefficient stress redistributions under mechanical loading. As a result, microstructural imperfections and flaws readily become crack initiation sites once the applied hoop stress surpasses the fracture threshold. This inability to dissipate strain energy promotes the simultaneous nucleation of multiple cracks, leading to a higher crack density [8,58,59]. Additionally, for their materials at 345 °C, a higher angle range of coating cracks was found against the hoop direction: 75° to 109° *vs.* 81° to 96° [4]. One potential reason could be the higher residual stresses in their Cr coating [21,56,57]. The interaction between the relaxation of such higher stress, and the applied mechanical loading induces a more complex stress distribution in the coating [62,63], and consequently results in more deviation of crack pathways. Therefore, as mentioned in Section 4.3, investigation of the residual stress distribution inside the Cr coating will be carried out in the future.

For materials tested at 650 °C, coating cracks formed in a ductile mode. Once the three coating cracks formed, further loading did not induce the formation of more coating cracks but increased the width of the existing coating cracks from ~8 μm to ~20 μm. This indicates that the brittle-to-ductile transition temperature (BDTT) of the PVD Cr coating could be in the range of 345 °C to 650 °C. It was suggested that the BDTT of Cr coating can be significantly affected by its microstructures and heat treatment processes [68–70]. For similar PVD Cr coatings, such BDTT is reported in the range of 400 °C to 450 °C [12,43]. For a more comprehensive understanding of the temperature-dependent of such cladding materials, future experiments incorporating intermediate temperature steps to determine the BDTT of current materials should be conducted.

For materials tested at 950 °C, it is noteworthy that a brittle failure mode was observed in the Cr coating (Fig. 11), despite the testing temperature is above the BDTT of the current PVD Cr coating (345 °C to 650 °C). Such ductile-to-brittle fracture could be caused by the increase of Cr grain sizes at high temperatures. The IPFs figure of Cr coating in materials after testing at 950 °C is presented in Fig. 14a with large column Cr grains can be found.

The distribution of the area of Cr grains were presented in Fig. 14b, where ~10 % of the Cr grains have an area of ~19.8 μm^2. The average area of Cr grains after testing at 950 °C is measured to be ~5.7 μm^2: ~4.2 times higher than the as-received materials (~1.1 μm^2). These all indicate the growth of Cr grains at 950 °C in current study. Similar phenomena has been reported by Liu et al. [71], they annealed Fe-6.5wt.%Si alloy at 950 °C for 30 mins, the grain sizes increase from 91 μm (as-received materials) to 255 μm. They suggested that larger grain sizes at high temperature result in an increased density of dislocations distributed in each grain [72], and such significant stress concentration could enhance the ability of transgranular cracking at lower levels of plastic deformation and consequently results in the brittle fracture mode. Such transgranular cracks were identified on the coating surface (Fig. 12b) at 950 °C in current work, and were not captured at other temperatures. Therefore, at 950 °C, recrystallisation of PVD Cr grains could occur, which resulted in the growth of Cr grains [36], concentrated stress in each grain, and eventually caused the transgranular cracks and brittle behaviour of the coating.

Lastly, as reported by Kim et al. [73], for PVD Cr-coated Zircaloy cladding under compressive loading, the initial coating cracks could concentrate stress towards the underlying substrate, and subsequently lead to cracks formed in the substrate. Upon these cracks reaching a critical penetration depth, the cracks undergo unstable propagation, resulting in the catastrophic failure of the entire coated cladding system. To further verify whether crack propagation is arrested at the coating/substrate interface, cross-sectional characterisation—such as focused ion beam (FIB) milling combined with SEM imaging—will be conducted in future work.

5. Conclusions

The microstructures, local properties and the failure processes of one PVD Cr-coated Opt. ZIRLO™ cladding materials were systematically studied. Crack initiation and propagation under C-ring compression at various temperatures (RT, 345 °C, 650 °C, and 950 °C) were analysed using real-time 3D XCT imaging. Nanoindentation and SEM imaging were employed to characterise the variation of local properties, microstructures, and crack patterns, supporting the interpretation of XCT observations.

For the as-received materials, smaller Cr grains close to coating-substrate interface exhibited higher hardness than the larger columnar grains in the middle of coating. Local property variations in coating and substrate were potentially attributed to high-temperature

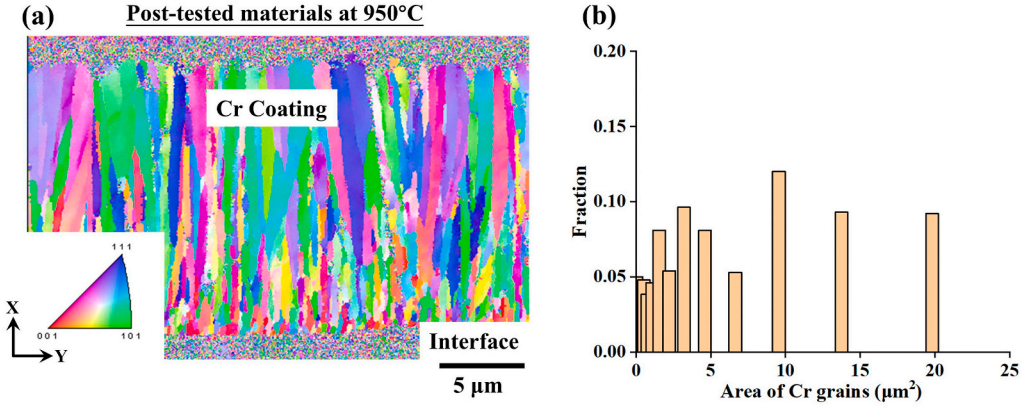

Fig. 14. Cr coating after tested at 950 °C: (a) IPFs figure of Cr coating and (b) distribution of area of Cr grains inside the coating.

recrystallisation, which enlarged grain size and caused coalescence of finer grains, affecting mechanical behaviour. Relaxation of residual stresses at elevated temperatures also likely contributed.

Load-displacement curves showed an initial linear stage at RT and 345 °C. Coating failure strain/stress was influenced by microstructure, local properties, and residual stress distributions. Significant strength degradation of the cladding materials was observed at 650 °C and 950 °C.

Temperature-dependent failure processes were investigated at elevated temperatures. At RT coatings fractured brittlely, multiple coating cracks formed simultaneously, with number of cracks increased with loading. Cracks propagated almost perpendicular to the hoop direction. At 345 °C, coating fractured in a more ductile behaviour, with lower number of cracks, and higher width of crack on the coating surface. However, a ductile fracture mode was observed at 650 °C, with cracks growing in width rather than number, indicating a brittle-to-ductile transition between 345 °C and 650 °C. Furthermore, coatings fractured brittlely again at 950 °C. Such ductile to brittle transition fracture mode at extreme temperatures could potentially be caused by the increasing of Cr grain sizes during recrystallisation, which concentrated stress in each grain and ultimately led to the brittle behaviour of the coating.

In summary, PVD Cr-coated cladding materials exhibit distinct temperature-dependent mechanical behaviours and failure processes under C-ring compression. These findings are essential for understanding their performance and guiding the design of advanced cladding materials for nuclear applications.

CRediT authorship contribution statement

Guanjie Yuan: Writing – original draft, Investigation, Formal analysis. **Martin Ševeček:** Writing – review & editing, Resources, Methodology. **David Cook:** Conceptualization. **Dula Parkinson:** Resources. **Robert O. Ritchie:** Resources, Methodology, Funding acquisition, Conceptualization. **Dong Liu:** Writing – review & editing, Resources, Methodology, Funding acquisition, Conceptualization.

Declaration of competing interest

The authors declare that they have no known competing financial interests or personal relationships that could have appeared to influence the work reported in this paper.

Acknowledgements

D.L. acknowledges funding support from UK EPSRC (EP/T000368/1), M.S. acknowledges funding support for the Centre of Advanced Nuclear Technology II (TN02000012) provided by the Technology Agency of the Czech Republic. The authors also acknowledge the use of the X-ray synchrotron micro-tomography beamline (8.3.2) at the Lawrence Berkeley National Laboratory's Advanced Light Source, which is supported by the Office of Science of the U.S. Department of Energy under contract no. DE-AC02-05CH11231.

Appendix A. Supplementary data

Supplementary data to this article can be found online at https://doi.org/10.1016/j.surfcoat.2025.132376.

Data availability

Data will be made available on request.

References

[1] K.A. Terrani, Accident tolerant fuel cladding development: promise, status, and, J. Nucl. Mater. 501 (2018) 13–30, https://doi.org/10.1016/j.jnucmat.2017.12.043.
[2] G.P. Sabol, G.R. Kilp, M.G. Balfour, E. Roberts, Development of a cladding alloy for high burnup, ASTM STP 1023 (1989) 227–244.
[3] J. Foster, H. Yueh, R. Comstock, Zirlo cladding improvement, J. ASTM Int. 5 (7) (2008) JAI101188.
[4] G. Yuan, et al., Materials & design in situ X-ray computed micro-tomography imaging of failure processes in Cr-coated Zircaloy nuclear fuel cladding materials, Mater. Des. 234 (May) (2023) 112373, https://doi.org/10.1016/j.matdes.2023.112373.
[5] G. Yuan, et al., Materials & design in situ high-temperature 3D imaging of the damage evolution in a SiC nuclear fuel cladding material, Mater. Des. 227 (2023) 111784, https://doi.org/10.1016/j.matdes.2023.111784.
[6] Shannon Bragg-Sitton, Development of advanced accident-tolerant fules for commercial LWRs, Nucl. News (2014) 83–91, no. March.
[7] M. Steinbrück, Oxidation of zirconium alloys in oxygen at high temperatures up to 1600 °C, Oxid. Met. 70 (5–6) (2008) 317–329, https://doi.org/10.1007/s11085-008-9124-z.
[8] H. Miwa, M. Amaya, The effect of oxidation-and-quenching process during a LOCA on the behavior of the oxidation and embrittlement of Zircaloy-4 cladding under reheating transients, J. Nucl. Sci. Technol. 53 (12) (Dec. 2016) 2090–2097, https://doi.org/10.1080/00223131.2016.1198730.
[9] J. Desquines, C. Duriez, S. Guilbert, T. Taurines, High temperature oxidation and room temperature axial strength of pre-oxidized zircaloy-4 cladding after a simulated LOCA, J. Nucl. Mater. 543 (Jan. 2021) 152559, https://doi.org/10.1016/j.jnucmat.2020.152559.
[10] H. Chen, X. Wang, R. Zhang, Application and development Progress of Cr-based surface coatings in nuclear fuel element: I. Selection, preparation, and characteristics of coating materials, Coatings 10 (9) (Aug. 2020) 808, https://doi.org/10.3390/coatings10090808.
[11] J. Brachet, et al., Early studies on Cr-coated Zircaloy-4 as enhanced accident tolerant nuclear fuel claddings for light water reactors, J. Nucl. Mater. 517 (2019) 268–285, https://doi.org/10.1016/j.jnucmat.2019.02.018.
[12] J. Jiang, et al., Temperature-dependent deformation and cracking behavior in Cr coating for accident tolerant fuel cladding : an in situ SEM study, Surf. Coat. Technol. 427 (August) (2021) 127815, https://doi.org/10.1016/j.surfcoat.2021.127815.
[13] J. Jiang, et al., In-situ study on the tensile behavior of Cr-coated zircaloy for accident tolerant fuel claddings, Surf. Coat. Technol. 394 (April) (2020) 125747, https://doi.org/10.1016/j.surfcoat.2020.125747.
[14] A.S.H. Makhlouf, Current and advanced coating technologies for industrial applications, Woodhead Publishing Limited, 2011, https://doi.org/10.1533/9780857094902.1.3.
[15] J.L. Míguez, L. Fernandes, A critical review on the numerical simulation related to physical vapour deposition, Procedia Manuf. 17 (2018) 860–869, https://doi.org/10.1016/j.promfg.2018.10.138.
[16] J.D. Hong, et al., Measurement of local mechanical properties for Cr-coated accident tolerant fuel cladding, J. Nucl. Mater. 579 (2023), https://doi.org/10.1016/j.jnucmat.2023.154407.
[17] M. Ghasabian, S. Talebi, F. Mofidnakhaei, Effect of gap design pressure on the LWR fuel rods lifetime, Kerntechnik 86 (3) (2021) 202–209, https://doi.org/10.1515/kern-2021-0004.
[18] S. Graff, et al., New LOCA and RIA fuel safety criteria in France, 2024, pp. 0–12.
[19] D. Kamerman, et al., Development of axial and ring hoop tension testing methods for nuclear fuel cladding tubes, Nucl. Mater. Energy 31 (March) (2022) 0–2, https://doi.org/10.1016/j.nme.2022.101175.
[20] W.C. Oliver, G.M. Pharr, An improved technique for determining hardness and elastic modulus using load and displacement sensing indentation experiments, J. Mater. Res. 7 (6) (1992) 1564–1583, https://doi.org/10.1557/JMR.1992.1564.
[21] K. Quillin, H. Yeom, T. Dabney, E. Willing, K. Sridharan, Microstructural and nanomechanical studies of PVD Cr coatings on SiC for LWR fuel cladding applications, Surf. Coat. Technol. 441 (April) (2022) 128577, https://doi.org/10.1016/j.surfcoat.2022.128577.
[22] Y. Liu, I. Bhamji, P.J. Withers, D.E. Wolfe, A.T. Motta, M. Preuss, Evaluation of the interfacial shear strength and residual stress of TiAlN coating on ZIRLO™ fuel cladding using a modified shear-lag model approach, J. Nucl. Mater. 466 (2015) 718–727, https://doi.org/10.1016/j.jnucmat.2015.06.003.
[23] ASTM Standard C1323-26, Standard Test Method for Ultimate Strength of Advanced Ceramics with Diametrally Compressed C-Ring Specimens at Ambient Temperature, ASTM International, West Conshohocken, PA, 2016, https://doi.org/10.1520/C1323-16.2.
[24] T.L. Embree, A.E. Segall, Evaluation of the uniaxiality of the stress state in C-ring fracture strength specimens, J. Test. Eval. 32 (2) (2004) 153–160, https://doi.org/10.1520/jte11965.
[25] D. Liu, et al., Damage tolerance of nuclear graphite at elevated temperatures, Nat. Commun. 8 (May) (2017) 1–9, https://doi.org/10.1038/ncomms15942.
[26] A. Haboub, et al., Tensile testing of materials at high temperatures above 1700°C with in situ synchrotron X-ray micro-tomography, Rev. Sci. Instrum. 85 (8) (2014), https://doi.org/10.1063/1.4892437.
[27] H.A. Bale, et al., Real-time quantitative imaging of failure events in materials under load at temperatures above 1,600°C, Nat. Mater. 12 (1) (2013) 40–46, https://doi.org/10.1038/nmat3497.

[28] L. Riviere, A wide-field micro-computed tomography detector : micron resolution at half-centimetre scale research papers, 2022, pp. 505–514, https://doi.org/10.1107/S160057752101287X.
[29] F. De Carlo, X. Xiao, C. Jacobsen, Research papers TomoPy: a framework for the analysis of synchrotron tomographic data research papers, 2014, pp. 1188–1193, https://doi.org/10.1107/S1600577514013939.
[30] T. Ferreira, W. Rasband, ImageJ user guide user guide ImageJ, Image J User Guide 1.46r (2012), https://doi.org/10.1038/nmeth.2019.
[31] ThermoFisher Scientific, Avizo 9 user's guide, in: Thermo Sci. Avizo Softw. 9 User's Guide, 2018, pp. 96–99.
[32] D. Vinh Nguyen, M. Le, L. Gélébart, J. Brachet, Mechanical behavior of a chromium coating on a zirconium alloy substrate at room temperature, J. Nucl. Mater. 558 (2022) 153332, https://doi.org/10.1016/j.jnucmat.2021.153332.
[33] R.V. Umretiya, et al., Mechanical and chemical properties of PVD and cold spray Cr-coatings on Zircaloy-4, jnucmat 541, 2020, pp. 50–65, https://doi.org/10.1016/j.jnucmat.2020.152420.
[34] Kim, D. and Lee, Y. Diffusion of chromium of Cr-coated Zircaloy accident tolerant fuel cladding: model development and experimental validation. Surf. Coat. Technol., 468, p. 129-698, https://doi.org/10.1016/j.surfcoat.2023.129698.
[35] V. Tuli, A. Claisse, L. Messina, P.A. Burr, Solubility and vacancy-mediated inter-diffusion in the Zr-Nb-Cr system, J. Nucl. Mater. 548 (2021), https://doi.org/10.1016/j.jnucmat.2021.152867.
[36] B. Li, et al., Thermal stability of the Cr-coated zirconium alloy microstructure prepared by pulsed laser deposition, Tungsten 6 (2) (2024) 333–341, https://doi.org/10.1007/s42864-023-00235-z.
[37] J. Yang, et al., High temperature Cr-Zr interaction of two types of Cr-coated Zr alloys in inert gas environment, J. Nucl. Mater. 547 (Apr. 2021) 152806, https://doi.org/10.1016/j.jnucmat.2021.152806.
[38] J.C. Brachet, et al., High temperature steam oxidation of chromium-coated zirconium-based alloys: kinetics and process, Corros. Sci. 167 (February) (2020), https://doi.org/10.1016/j.corsci.2020.108537.
[39] H. Nakajima, The discovery and acceptance of the Kirkendall effect: the result of a short research career, Jom 49 (6) (1997) 15–19, https://doi.org/10.1007/BF02914706.
[40] K.J. Dawson, et al., Physical vapor deposition as a route to hidden amorphous states, Proc. Natl. Acad. Sci. U. S. A. 106 (36) (2009) 15164–15170, https://doi.org/10.1073/pnas.0901469106.
[41] A. Fazi, K. Stiller, H.-O. Andrén, M. Thuvander, Cold sprayed Cr-coating on optimized ZIRLO™ claddings: the Cr/Zr interface and its microstructural and chemical evolution after autoclave corrosion testing, J. Nucl. Mater. 560 (Mar. 2022) 153505, https://doi.org/10.1016/j.jnucmat.2022.153505.
[42] W. Wang, et al., Construction of Cr coatings with different columnar structure on Zircaloy-4 alloys to optimize the high-temperature steam oxidation behavior for accident tolerant fuel claddings, J. Alloys Compd. 946 (2023) 169385, https://doi.org/10.1016/j.jallcom.2023.169385.
[43] J. Jiang, et al., Surface & coatings technology comparative study on the tensile cracking behavior of CrN and Cr coatings for accident-tolerant fuel claddings, Surf. Coat. Technol. 409 (January) (2021) 126812, https://doi.org/10.1016/j.surfcoat.2020.126812.
[44] G. Pinto, Sputtering physical vapour deposition (PVD) coatings: a critical review on process improvement and market trend demands, Coatings (2018), https://doi.org/10.3390/coatings8110402.
[45] A.J. Leide, et al., Measurement of residual stresses in surrogate coated nuclear fuel particles using ring-core focussed ion beam digital image correlation, Nucl. Mater. Energy 36 (2023) 101470, https://doi.org/10.1016/j.nme.2023.101470.
[46] S. Hoshino, H.A. Laitinen, G.B. Hoflund, The electrodeposition and properties of amorphous chromium films prepared from chromic acid solutions, J. Electrochem. Soc. 133 (4) (1986) 681–685, https://doi.org/10.1149/1.2108653.
[47] P. Yi, Low temperature annealing of a cold worked Zr-Nb alloy, J. Phys. Conf. Ser. 1676 (1) (2020), https://doi.org/10.1088/1742-6596/1676/1/012176.
[48] Y. lan, et al., Microstructure evolution and recrystallization behavior of cold-rolled Zr-1Sn-0.3Nb-0.3Fe-0.1Cr alloy during annealing, Trans. Nonferrous Met. Soc. China Engl. Ed. 28 (4) (2018) 651–661, https://doi.org/10.1016/S1003-6326(18)64697-7.
[49] C. Song, et al., Microstructural and mechanical property evolution of a nuclear zirconium-4 alloy fabricated via laser powder bed fusion and annealing heat treatment, Virtual Phys. Prototyp. 18 (1) (2023), https://doi.org/10.1080/17452759.2023.2189597.
[50] C. National, D.E. Atbmica, B. Aires, Tensile properties of Zircaloy-4 67 (1977) 198–206.
[51] Z. Zhao, et al., Mechanical properties of Zircaloy-4 cladding tube by advanced expansion due to compression (A-EDC) test, Mater. Trans. 58 (1) (2017) 46–51, https://doi.org/10.2320/matertrans.ML201601.
[52] M. Le Saux, et al., Behavior and failure of uniformly hydrided Zircaloy-4 fuel claddings between 25°C and 480°C under various stress states, including RIA loading conditions, Eng. Fail. Anal. 17 (3) (Apr. 2010) 683–700, https://doi.org/10.1016/j.engfailanal.2009.07.001.
[53] S.B. Bell, et al., In-situ determination of strain during transient burst testing and the temperature dependence of Zircaloy-4 claddings, J. Nucl. Mater. 591 (Apr. 2024) 154910, https://doi.org/10.1016/j.jnucmat.2024.154910.
[54] R.B. Adamson, C.E. Coleman, M. Griffiths, Irradiation creep and growth of zirconium alloys: a critical review, J. Nucl. Mater. 521 (Aug. 2019) 167–244, https://doi.org/10.1016/j.jnucmat.2019.04.021.
[55] N. Hansen, Hall–Petch relation and boundary strengthening, Scr. Mater. 51 (8) (Oct. 2004) 801–806, https://doi.org/10.1016/j.scriptamat.2004.06.002.
[56] O.B. Soroka, Evaluation of residual stresses in PVD-coatings. Part 1. Review, Strength Mater. 42 (3) (May 2010) 287–296, https://doi.org/10.1007/s11223-010-9217-1.
[57] H. Lille, et al., Residual stresses on various PVD hard coatings on tube and plate substrates, Coatings 10 (11) (Oct. 2020) 1054, https://doi.org/10.3390/coatings10111054.
[58] T. Guo, et al., Cleavage cracking of ductile-metal substrates induced by brittle coating fracture, Acta Mater. 152 (Jun. 2018) 77–85, https://doi.org/10.1016/j.actamat.2018.04.017.
[59] B. Yang, et al., Measurement of fracture toughness and interfacial shear strength of hard and brittle Cr coating on ductile steel substrate, Surf. Eng. 24 (5) (2008) 332–336, https://doi.org/10.1179/174329408X282587.
[60] J. Jiang, et al., Temperature-dependent deformation and cracking behavior in Cr coating for accident tolerant fuel cladding: an in situ SEM study, Surf. Coat. Technol. 427 (Dec. 2021) 127815, https://doi.org/10.1016/j.surfcoat.2021.127815.
[61] Z. Xu, J. Wei, Y. Liu, B. Wang, The effect of oblique crack on stability and fracture properties of Cr-coated Zircaloy cladding, Ann. Nucl. Energy 163 (Dec. 2021) 108560, https://doi.org/10.1016/j.anucene.2021.108560.
[62] K. Quillin, et al., Microstructural and nanomechanical studies of PVD Cr coatings on SiC for LWR fuel cladding applications, Surf. Coat. Technol. 441 (Jul. 2022) 128577, https://doi.org/10.1016/j.surfcoat.2022.128577.
[63] S. Zeng, et al., Improved oxidation resistance of Cr-Si coated Zircaloy with an in-situ formed Zr2Si diffusion barrier, Npj Mater. Degrad. 7 (1) (Jul. 2023) 56, https://doi.org/10.1038/s41529-023-00373-2.
[64] D.W. Green, M.Z. Southard, Perry's chemical engineers' handbook, McGraw-Hill Education, 2019.
[65] W.M. Haynes, CRC handbook of chemistry and physics, CRC press, 2016.
[66] A. Hellouin, et al., Hydrogen contribution to the thermal expansion of hydrided Zircaloy-4 cladding tubes, J. Nucl. Mater. 440 (1–3) (2013) 169–177, https://doi.org/10.1016/j.jnucmat.2013.04.039.
[67] O. Zanellato, et al., Synchrotron diffraction study of dissolution and precipitation kinetics of hydrides in Zircaloy-4, J. Nucl. Mater. 420 (1–3) (2012) 537–547, https://doi.org/10.1016/j.jnucmat.2011.11.009.
[68] Z. Alam, et al., Micromechanisms of fracture and strengthening in free-standing Pt-aluminide bond coats under tensile loading, Acta Mater. 67 (2014) 278–296, https://doi.org/10.1016/j.actamat.2013.12.033.
[69] R. Wadsack, The effect of pre-deformation on the ductility of chromium 311 (2002) 701–704.
[70] U. Holzwarth, H. Stamm, Mechanical and thermomechanical properties of commercially pure chromium and chromium alloys, J. Nucl. Mater. 300 (2002) 161–177.
[71] Y. Liu, et al., Effect of grain size and grain boundary on ductile to brittle transition behavior of Fe-6.5wt.%Si alloy under miniaturized three-point bending tests, Mater. Lett. 353 (July) (2023) 135288, https://doi.org/10.1016/j.matlet.2023.135288.
[72] F.C. Salvado, et al., A review on the strain rate dependency of the dynamic viscoplastic response of FCC metals, Prog. Mater. Sci. 88 (2017) 186–231, https://doi.org/10.1016/j.pmatsci.2017.04.004.
[73] J. Kim, S. Joung, Y. Lee, Effect of Cr coating on the mechanical integrity of accident tolerant fuel cladding under ring compression test, J. Nucl. Mater. 585 (Nov. 2023) 154603, https://doi.org/10.1016/j.jnucmat.2023.154603.